J. Fluid Mech. (2012), *vol.* 694, *pp.* 225–251.
doi:10.1017/jfm.2011.540

Ice ripple formation at large Reynolds numbers

Carlo Camporeale† and Luca Ridolfi

Department of Water Engineering, Politecnico di Torino, Corso Duca degli Abruzzi, 24, 10129 Torino, Italy

(Received 11 April 2011; revised 30 September 2011; accepted 9 December 2011; first published online 2 February 2012)

A free-surface-induced morphological instability is studied in the laminar regime at large Reynolds numbers ($Re = 1$–10^3) and on sub-horizontal walls ($\vartheta < 30°$). We analytically and numerically develop the stability analysis of an inclined melting–freezing interface bounding a free-surface laminar flow. The complete solution of both the linearized flow field and the heat conservation equations allows the exact derivation of the upper and lower temperature gradients at the interface, as required by the Stefan condition, from which the dispersion relationship is obtained. The eigenstructure is obtained and discussed. Free-surface dynamics appears to be crucial for the triggering of upstream propagating ice ripples, which grow at the liquid–solid interface. The kinematic and the dynamic conditions play a key role in controlling the formation of the free-surface fluctuations; these latter induce a streamline distortion with an increment of the wall-normal velocities and a destabilizing phase shift in the net heat transfer to the interface. Three-dimensional effects appear to be crucial at high Reynolds numbers. The role of inertia forces, vorticity, and thermal boundary conditions are also discussed.

Key words: channel flow, morphological instability, solidification/melting

1. Introduction

This study investigates the morphological instability of a liquid–solid interface bounding a laminar open-channel flow at large Reynolds numbers. The onset of turbulence is the most celebrated kind of instability in shear flows at high Reynolds numbers, and motivated the earliest theoretical investigations through the use of normal (Drazin & Reid 1981) and non-normal (Schmid & Henningson 2001) temporal modes. As this hydrodynamic instability is the typical evidence of the unstable character of Navier–Stokes equations, one could conjecture that any other form of flow-driven instability should be subordinate to the turbulence occurrence. This is instead not always true: e.g. it is well known that, in free-surface flows, unstable surface waves also develop in laminar conditions (e.g. Benjamin 1957; Yih 1963; Wierschem & Aksel 2003). However, in the context of morphodynamic instabilities, where a shear flow mutually interacts with a deformable wall, the above conjecture has found wide consensus in the past.

For instance, the instability developed on soluble surfaces has been found to support the hypothesis that scalloping is due to the imprint of coherent structures typical of wall turbulence (Blumberg & Curl 1974). The analysis by Thomas (1979) extended

† Email address for correspondence: carlo.camporeale@polito.it

such a wall-similarity hypothesis to other geophysical and industrial flows (such as interactions with granular beds, colloidal particles, dissolution patterns and phase change processes). This empirical evidence has implicitly reinforced the conjecture that no instabilities form on deformable walls that are bounded by a laminar flow, in particular in two branches of morphodynamics that are very close to each other: Exner-like and Stefan-like problems.

In Exner-like problems, the deformable wall is represented by a non-cohesive granular bed and the interfacial boundary equation is a continuity equation for the sediment phase, called the Exner equation (Exner 1925). In this context, the assumption that ripples and dunes can form only with a turbulent flow has been controverted only recently both by experiments (Coleman & Edling 2000) and by theoretical analyses (Devauchelle *et al.* 2010), where sand wavelet formation was revealed beneath a sub-critical laminar open-channel flow.

In Stefan-like problems, the deformable wall is a freezing–melting interface governed by the heat-flow conservation equation, namely the Stefan condition (Stefan 1891). These problems find several applications, such as the formation and growth of river and sea ice covers (Ashton & Kennedy 1972; Feltham & Worster 1999), supra-glacial melting, freezing in a water pipe flow (Gilpin 1981), solidification of binary alloys in the production of semi-conducting crystals (Worster 2000), icicle formation (Ueno 2003; Neufeld, Goldstein & Worster 2010; Ueno *et al.* 2010). The experiments by Gilpin and co-workers (Gilpin, Hirata & Cheng 1980; Gilpin 1981) and the theoretical model developed by Thorsness & Hanratty (1979) have, in particular, emphasized that the essential mechanism for the formation of an ice-band structure (i.e. the occurrence of a flow-induced wall instability) is the effect of flow acceleration on turbulence structure.

However, the assumptions that turbulence is an essential requisite of instability for Stefan-like problems was controverted by the seminal works by Ogawa & Furukawa (2002) and Ueno (2003), where icicle instability was investigated in the Stokes regime ($Re < 1$) for near-vertical walls. Most recently, Short, Baygents & Goldstein (2006) and Neufeld *et al.* (2010) have emphasized that this latter kind of instability is regulated by the convective boundary layer in the air surrounding icicles, rather than heat transport in the liquid film.

As far as sub-horizontal walls are concerned, Feltham & Worster (1999) showed that a laminar liquid flow in a semi-infinite region induces an instability of a mush-melt interface; however, they found that the liquid–solid interface is stable if the mushy layer is absent. To date, no theoretical analysis has been formulated yet for the stability of a freezing–melting interface that bounds a laminar open-channel flow at large Reynolds numbers (say, $Re = 1–10^3$), where inertial effects are not negligible. This is the reason for the present work, where we will limit the case to sub-horizontal walls (i.e. the slope $\vartheta < 30°$), in order to neglect the natural convection of air.

Due to measurement requirements, the experiments by Gilpin *et al.* (1980) were conducted with the presence of a free surface, but back-water effects were not negligible, and the authors focused their analysis on the turbulent regime. Indeed, it should also be noticed that a Stefan-like experimental study, involving a laminar open-channel flow, would entail even more practical problems than the Exner counterpart. This is because of the difficulty involved in achieving an initial equilibrium condition at the basic state (i.e. a stable flat solid–liquid interface). A fully analytical stability analysis is instead more likely to be successful with respect to Exner-like problems. In fact, while in this latter case the grain–flow interaction adds complexity and usually requires empirical closures, the liquid–solid interface instability is driven by

a convective–diffusive heat flux that can be studied through exact conservation laws (Hutter 1983).

We will show that, under well-defined flow conditions, unstable ice waves (which we will name ice ripples) develop on the liquid–solid interface, in an apparently similar way to the classical ripple formation occurring on sand beds. The key mechanism is found to be related to the kinematic distortion of the heat flux caused by the free surface fluctuations. In particular, the free surface seems to be the necessary element for instability to occur, even for walls of very low slopes and without any mushy layer. This is due to the fact that the upper and lower boundaries (namely the free surface and the liquid–solid interface) mutually interact with the hydrodynamic and thermodynamic structure of the flow, by means of suitable boundary conditions. In this sense, we connect the consolidated knowledge of gravity-driven flows of a viscous film (e.g. Wang 1981; Luo & Pozrikidis 2006) with the above illustrated Stefan-like problems. Furthermore, we show that Squire's theorem cannot be extended to the present problem, since at large Reynolds number three-dimensional patterns become more unstable than their two-dimensional counterparts.

The above thermo-fluid-dynamic problem finds an interesting application in glacier hydrology. It is well known that post-1970 global warming is inducing a generalized mass reduction of glaciers. Kaser *et al.* (2006) reported an average mass balance of -283 ± 123 kg m^{-2} y^{-1} for 1961–2004, excluding peripheral ice bodies in Greenland and Antarctica, and -510 ± 100 kg m^{-2} y^{-1} for 2001–2004 (corresponding to nearly 1 mm sea-level equivalent per year). During the melting season, snow cover is therefore likely to be absent and ice is directly exposed to meltwater. If the surface slope is small, so that the glacier has few crevasses, a complex and variegated set of morphological patterns, induced by spatial gradients in freezing and melting, develop on the ice surface. One of the best known of these structures is 'bediers', also called supraglacial rivers, which convey most of the meltwater and usually develop a meandering dynamics (e.g. Ferguson 1973; Parker 1975). In this way, the glacier surface performs a kind of hydrologic network (another similarity between Stefan- and Exner-like problems), whereby the whole balance of mass is greatly affected. Either in the upper zone of the glacier, where the meltwater is not yet channelized and a shallow (but non-vanishing) film of water is present, or on the bottom of bediers, one can also observe the formation of ice ripples, where a well-selected wavelength develops in the direction of the maximum slope of the bed. Figure 1 shows the pattern of ice ripples left by the flow, as observed during field work on the Ciardoney glacier (Italy) carried out in September 2006. It can be observed that the pattern is aligned with the main slope of the surface, being the direction of the surface melt flow.

2. Problem formulation

2.1. *Governing equations*

We consider a single-component two-phase system, where a free-surface viscous liquid flows over a base solid surface at the melting point, which, in the absence of corrugations, is inclined at the angle ϑ (see figure 2). Let us introduce the right-handed Cartesian reference frame, $\tilde{\boldsymbol{x}} \equiv \{\tilde{x}, \tilde{y}, \tilde{z}\}$, where the $\tilde{x}$-axis is tangent to the base plane (spanned by the vector $\tilde{\boldsymbol{x}}_h \equiv \{\tilde{x}, \tilde{y}\}$) and parallel to the direction of the maximum slope, and the $\tilde{z}$-axis is orthogonal to the base plane and points upwards. Accordingly, $\tilde{u}$, $\tilde{v}$ and $\tilde{w}$ are the components of the velocity vector $\boldsymbol{u}(\tilde{\boldsymbol{x}}, \tilde{t})$. Henceforth, the tilde refers to the dimensional variables, subscripts L and S mark the liquid and the solid phase, and subscripts F, I and B refer to the liquid free surface, the liquid–solid

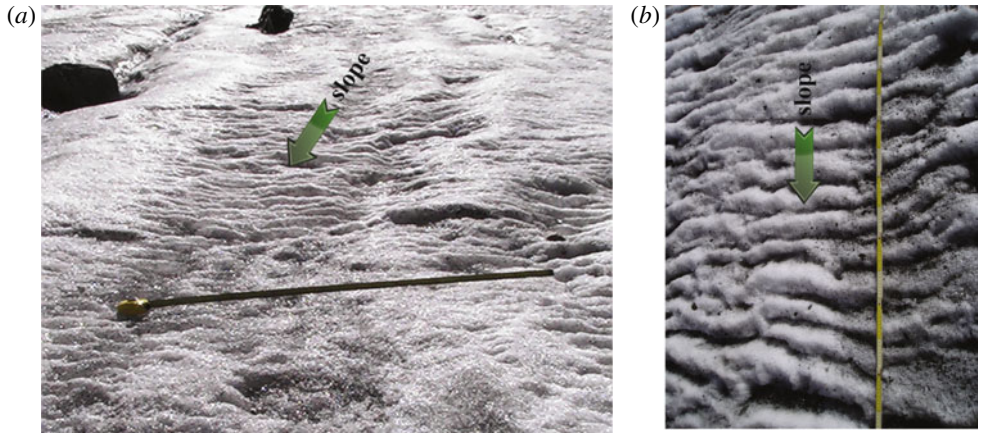

FIGURE 1. (Colour online available at journals.cambridge.org/flm) (*a*) Ice ripples on the upper surface of the Ciardoney glacier (North Italy, 45°31′N–7°23′E; altitude: 3100 m). The arrows indicate the slope of the bed. The 1 m rule gives the scale of the picture. (*b*) Close-up of (*a*). Slope, $\vartheta = 5°–10°$. Longitudinal and transversal wavelengths are ∼0.1 and 1 m, respectively. Other data and pictures can be found on the website: http://www.nimbus.it/ghiacciai/2006/060915ciardoney.htm.

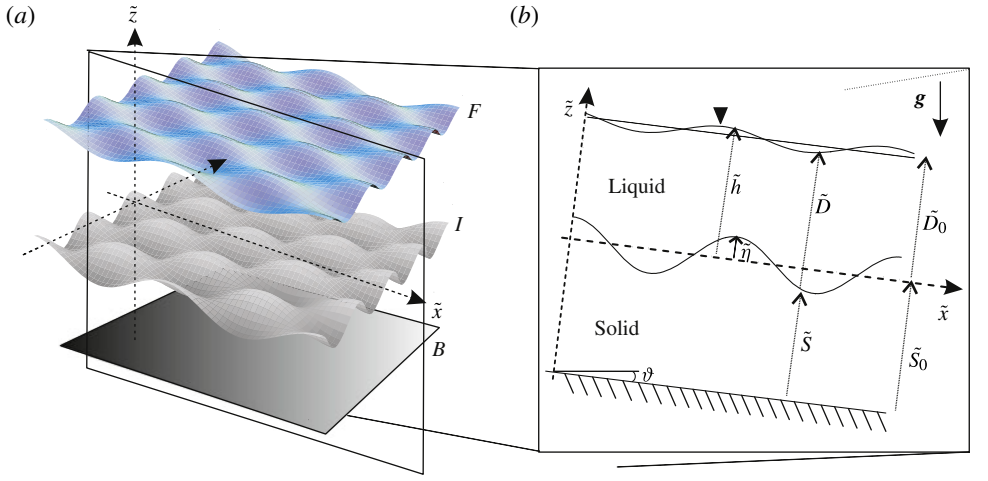

FIGURE 2. (Colour online) Sketch of the physical system. (*a*) Three-dimensional view; (*b*) longitudinal section. Letters F, I and B refer to the liquid free surface, the liquid–solid interface, and the bottom of the solid phase, respectively.

interface, and the bottom of the solid phase, respectively. If the variables are made dimensionless using the surface velocity, $\tilde{U}_F$, the stream depth, $\tilde{D}_0$, in absence of corrugations, a characteristic time scale of the interface evolution, τ (see below), and the temperature difference, $\Delta = \tilde{T}_I - \tilde{T}_B$, one obtains the following dimensionless quantities:

$$(h, \eta, D, S) = \frac{(\tilde{h}, \tilde{\eta}, \tilde{D}, \tilde{S})}{\tilde{D}_0}, \quad p = \frac{\tilde{p}}{\rho_L \tilde{U}_F^2}, \quad \theta = \frac{\tilde{T} - \tilde{T}_I}{\Delta}, \tag{2.1a–c}$$

	Re	ϑ (deg.)	θ	Δ (K)	Fr	St	χ	$Ec\,Re^{-1}$	J	Ar
MIN	1	0.5	0.01	0.1	0.1	5×10^{-4}	10^{-8}	10^{-10}	10^{-7}	10^{-7}
MAX	10^3	30	1	50	20	0.3	0.015	10^{-6}	10^{-6}	10^{-5}

TABLE 1. Range of the pure numbers, being Re, ϑ, θ and Δ the independent parameters.

$$Re=\frac{\tilde{U}_F\tilde{D}_0}{\nu},\quad Fr=\frac{\tilde{U}_F}{\sqrt{g\tilde{D}_0}},\quad We=\tilde{U}_F\sqrt{\frac{\rho_L\tilde{D}_0}{\sigma}},\quad Ar=\frac{\varsigma\theta^F\Delta}{Fr^2},\qquad (2.2a\text{–}c)$$

$$Pe=\frac{\tilde{U}_F\tilde{D}_0}{\gamma_L},\quad Ec=\frac{\tilde{U}_F^2}{c_L\Delta},\quad St=\frac{c_S\Delta}{\lambda},\quad r_\kappa=\frac{\kappa_L}{\kappa_S},\quad r_\gamma=\frac{\gamma_L}{\gamma_S},\qquad (2.3a\text{–}e)$$

where $\tilde{\eta}(\tilde{\boldsymbol{x}}_h,\tilde{t})$ is the two-dimensional corrugation of the liquid–solid interface while $\tilde{h}(\tilde{\boldsymbol{x}}_h,\tilde{t})$, $\tilde{D}(\tilde{\boldsymbol{x}}_h,\tilde{t})$ and $\tilde{S}(\tilde{\boldsymbol{x}}_h,\tilde{t})$ are the free-surface elevation, the liquid and the solid depths, respectively; ρ is the density, $\tilde{p}\,(\tilde{\boldsymbol{x}},\tilde{t})$ is the pressure, $\tilde{T}(\tilde{\boldsymbol{x}},\tilde{t})$ is the temperature, ν is the kinematic viscosity of the liquid phase, $\boldsymbol{g}\equiv g(\sin\vartheta,0,-\cos\vartheta)$ is the gravity vector, κ is the thermal conductivity, σ is the surface tension, ς is the volumetric thermal expansion coefficient of the liquid, c is the specific heat capacity, λ is the latent heat of melting, and $\gamma=\kappa/\rho c$ is the thermal diffusivity. The dimensionless temperature ratio θ quantifies the relative difference between the actual temperature and the melting point, so that $\theta_I=0$ at the basic state (see below) and $\theta_B=-1$. Finally, Re, Fr, We, Ar, Pe, Ec and St are the Reynolds, Froude, Weber, Archimedes, Péclet, Eckert and Stefan numbers, respectively.

The following assumptions are assumed. (i) The fluid is incompressible. (ii) The flow is in laminar regime, namely $Re<750$. (iii) Gravity is the only external force. (iv) Buoyancy effects are neglected (i.e. $Ar\ll1$; see also table 1) and fluid characteristics are considered as constants (e.g. Worster 1992). (v) The liquid–solid interface is at dynamical thermal equilibrium, which means that the spatially averaged displacement, η, of the liquid–solid interface from the plane $z=0$ is zero. (vi) The fluid-dynamic response of the gas phase over the liquid free surface is neglected.

Assumption (iii) implies that the basic flow at the free surface is the vector $\{\tilde{U}_F,0,0\}$ (i.e. parallel to the x-axis), where $\tilde{U}_F$ follows the Nusselt solution, $\tilde{U}_F=g\sin\vartheta\tilde{D}_0^2/2\nu$. Hypothesis (iv) requires that the temperature difference between the free surface and the liquid–solid interface does not exceed a few degrees. From hypothesis (v)–(vi) it follows that, in the absence of bed corrugations, a fixed time-invariant relationship between the basic solid depth, $S_0=S-\eta$, and the basic free-surface temperature, θ_0^F, exists, namely $S_0=S_0(\theta_0^F)$ (see (2.15a)). These last two assumptions – along with the range of Reynolds numbers under consideration – preclude the study of icicles.

The liquid–solid interface is a surface of phase transition that is defined by equation $\mathscr{I}(\tilde{\boldsymbol{x}},\tilde{t})=\tilde{z}-\tilde{\eta}(\tilde{\boldsymbol{x}}_h,\tilde{t})=0$ (likewise, the free surface will be indicated with the notation $\mathscr{F}(\tilde{\boldsymbol{x}},\tilde{t})$). The accumulation (or the release) of the latent heat at the liquid–solid interface is caused by the net difference between the incoming and the outgoing heat flux and it is converted into melting (growing) of the liquid–solid interface. This thermal energy balance equation (i.e. the so-called Stefan condition) is given

by $\rho_S \lambda \xi = [\tilde{\boldsymbol{q}} \cdot \boldsymbol{n}_I]_S^L$, where $\xi = \tilde{\boldsymbol{x}}_{,\tilde{t}} \cdot \boldsymbol{n}_I$ is the displacement velocity of the surface $\mathscr{I}$ (the comma notation refers to the partial derivative), $\boldsymbol{n}_I = \boldsymbol{\nabla}\mathscr{I}/|\boldsymbol{\nabla}\mathscr{I}|$ is the unit normal vector pointing into the liquid film, and $\tilde{\boldsymbol{q}} = -\kappa \boldsymbol{\nabla}\tilde{T}$ is the Fourier heat flux vector. After straightforward algebraic manipulations, the dimensionless form of the Stefan condition reads

$$\frac{\rho_S \lambda \tilde{D}_0^2}{\tau \kappa_S \Delta} \eta_{,t} = [\boldsymbol{\nabla}\theta\,|^{\eta^-} - r_\kappa \boldsymbol{\nabla}\theta|_{\eta^+}] \cdot \boldsymbol{\nabla}\mathscr{I}. \tag{2.4}$$

Since (2.4) describes the spatio-temporal dynamics of the morphological instability, without any loss of generality we can assume the left-hand side to be of order one and, hence, $\tau = \tilde{D}_0^2 (\gamma_S S_t)^{-1}$.

The thermo-fluid-dynamic behaviour of the two-phase system under consideration is described by the conservation equations of mass (continuity equation), momentum (Navier–Stokes equations) and heat for the liquid and solid phase: namely,

$$\boldsymbol{\nabla} \cdot \boldsymbol{u} = 0, \quad \left(\chi \frac{\partial}{\partial t} + \boldsymbol{u} \cdot \boldsymbol{\nabla} - \frac{\nabla^2}{Re}\right) \boldsymbol{u} = -\boldsymbol{\nabla} p + \boldsymbol{\delta}, \quad (\eta \leqslant z \leqslant \eta + D), \tag{2.5}$$

$$\left[\chi \left(\frac{\partial}{\partial t} + s \frac{\partial \eta}{\partial t} \frac{\partial}{\partial z}\right) + \boldsymbol{u} \cdot \boldsymbol{\nabla} - \frac{\nabla^2}{Pe}\right] \theta = \frac{E_c}{Re} \Phi_d, \quad (\eta \leqslant z \leqslant \eta + D), \tag{2.6}$$

$$\left(S_t \frac{\partial}{\partial t} - \nabla^2\right) \theta = 0, \quad (-S \leqslant z < \eta), \tag{2.7}$$

where $\boldsymbol{\delta} = Fr^{-2}(\sin\vartheta, 0, -\cos\vartheta)$, $\chi = St\,(r_\gamma Pe)^{-1}$ characterizes the importance of hydrodynamic unsteadiness, Φ_d is the dissipation function due to the internal viscous stresses, and the term $s\eta_{,t}\theta_{,z}$ in (2.6) represents the expenditure of expansion work due to the density difference between the liquid and solid phase, with $s = 1 - \rho_S/\rho_L$ (e.g. Lock 1990). The following boundary conditions complete the mathematical problem:

$$\frac{\mathrm{D}\mathscr{F}}{\mathrm{D}t} = \frac{\mathrm{D}\mathscr{I}}{\mathrm{D}t} = 0, \quad (\boldsymbol{n} \cdot \boldsymbol{T} \cdot \boldsymbol{t})_F = 0, \quad (\boldsymbol{n} \cdot \boldsymbol{T} \cdot \boldsymbol{n})_F + \frac{Re}{We^2} \mathscr{K}_F = 0, \tag{2.8a–d}$$

$$(\boldsymbol{t} \cdot \boldsymbol{u})_I = 0, \quad \theta_I = -J\mathscr{K}_I, \quad \eta_{,t} = [1 - \theta_{,x}\eta_{,x} - \theta_{,y}\eta_{,y}]_{\eta^-} - r_\kappa\,[1 - \theta_{,x}\eta_{,x} - \theta_{,y}\eta_{,y}]_{\eta^+}, \tag{2.9a–c}$$

$$[\boldsymbol{n} \cdot \boldsymbol{\nabla}\theta]_{\eta^-} = r_\kappa\,[\boldsymbol{n} \cdot \boldsymbol{\nabla}\theta]_{\eta^+}, \quad [\theta_{,z}]_B = r_\kappa\,[\boldsymbol{n} \cdot \boldsymbol{\nabla}\theta]_F = S_0^{-1} \tag{2.10a,b}$$

where $\boldsymbol{n}$ and $\boldsymbol{t}$ are the unit normal and tangent vectors to a generic surface, respectively, $\boldsymbol{T} = p\,Re\,\boldsymbol{I} - 2\boldsymbol{D}$ is the dimensionless Newtonian stress tensor (with $\boldsymbol{I}$ and $\boldsymbol{D}$ the identity matrix and the rate-of-strain tensor, respectively), $\mathscr{K}_F = (1/2)[(\boldsymbol{I} - \boldsymbol{n}_F\boldsymbol{n}_F) \cdot \boldsymbol{\nabla}] \cdot \boldsymbol{n}_F$ is the local mean curvature of the free surface (while $\mathscr{K}_I$ is the corresponding value at the interface).

Equations (2.8*a–b*) are the kinematic condition for the free surface and liquid–solid interface, respectively, and force the two surfaces to be the upper and the lower border of the fluid domain. Equations (2.8*c–d*) state the tangential and normal components of momentum conservation at the free surface, i.e. the so-called dynamic conditions. We emphasize that the last term in (2.8*c*) takes into account the effect of the surface tension.

Equation (2.9*a*) stands for the no-slip condition, since the liquid is pure and there is no mushy layer (see instead Feltham & Worster 1999 for the case with a

mushy layer induced by a colloid but without a free surface). Equation (2.9*b*) is the Gibbs–Thomson formula, which states that the surface forces change the phase equilibria, causing the equilibrium freezing temperature to be depressed when the interface is convex towards the liquid (e.g. Worster 2000). It is straightforward to show that $J = r_\rho r_c r_T EcSt We^{-2}$ (where $r_\rho = \rho_L/\rho_S$, $r_c = c_L/c_S$, $r_T = 1 - \theta_B$). Equation (2.9*c*) is the Stefan boundary condition. Finally, (2.10*a*) states the heat flux continuity at the liquid–solid interface whereas (2.10*b*) states that the domain is entirely crossed by a constant heat flux, which in turn is not affected by the perturbed field. Despite the apparent arbitrariness of this latter condition, we will show at the end of § 5 that other choices do not change the results.

The above equations can be somewhat simplified by the order of magnitude analysis summarized in table 1 (corresponding to the case of an ice–water system), from which two considerations follow. First, the internal dissipation and the Gibbs–Thomson effect can always be neglected. Thus (2.9*b*) reduces to the standard Dirichlet boundary condition. Although the Gibbs–Thomson effect is the key mechanism that induces the wavenumber selection in the static morphological instability of the classic Stefan problem, it does not have any particular relevance in the hydrodynamic case.

Second, from the mathematical problem (2.5)–(2.10) different types of unsteadiness emerge, which we expect to be related to three sources of temporal instabilities: (i) the above-mentioned morphological mode (i.e. the main focus of the present analysis), which is driven by the Stefan equation and develops with a unitary time scale, if dimensionalized with τ; (ii) the (coupled) hydrodynamic and fluid-induced thermodynamic modes, driven by (2.5)–(2.6), respectively, with a time scale of order χ; (iii) the solid-induced thermodynamic mode, driven by the heat conservation in the solid phase, with a time scale of order St. Basically, type (i) is generally slower than types (ii) and (iii), so it is customary to assume that the flow field and temperature distribution quickly adjust to the slowly time-dependent configuration of the bottom. This is indeed a very common condition in morphodynamic problems (the so-called 'quasi-steady approximation'): for instance, in river dynamics, time evolution of sediment dunes, bars or meanders is much slower than the flow field evolution (e.g. Colombini & Stocchino 2005; Camporeale *et al.* 2007; Seminara 2010). Nonetheless, the upper bounds in the estimate of χ and St suggest that, under particular conditions, one could expect a contribution even from the unsteadiness of types (ii) and (iii). The fully numerical solution developed in § 3.2 will elucidate this aspect.

Finally, according to Yih (1963), when $Re \geqslant 1.25 \cot\vartheta$ the base flow becomes wavy because of the growth of a linear surface instability. This is indeed a fourth type of instability related to boundary conditions on the free surface, even though, in the linear approximation, the stability analysis of the liquid–solid interface is expected to be unaffected by surface instabilities, since the two phenomena are independent (Bontozoglou & Papapolymerou 1997).

2.2. *The eigenvalue problem*

The transformation of variables,

$$\zeta = \begin{cases} \dfrac{z - \eta(\boldsymbol{x}_h, t)}{D(\boldsymbol{x}_h, t)}, \\ \dfrac{z - \eta(\boldsymbol{x}_h, t)}{S(\boldsymbol{x}_h, t)}, \end{cases} \qquad (2.11a,b)$$

$$\theta = \begin{cases} \theta^L & (z \geqslant \eta), \\ \theta^S & (z < \eta), \end{cases} \tag{2.11c,d}$$

permits the domains $[-S, \eta]$ and $[\eta, \eta + D]$ to be mapped into two rectangular domains for the liquid ($\zeta \in [0, 1]$) and solid phases ($\zeta \in [-1, 0]$), respectively (see figure 2).

A linear stability analysis of the system in the three-dimensional domain, which takes into account the symmetry with respect to the x-axes (due to assumption (iii)), requires the system to be forced with a generic two-dimensional harmonic disturbance,

$$\eta = \hat{\varepsilon}\eta_1 \, \mathrm{e}^{\omega_r t} \cos(\alpha x + \omega_i t) \cos(\beta y), \tag{2.12}$$

where $\hat{\varepsilon}$ is the (small) amplitude of the corrugations of the surface $\mathscr{I}$, $\omega = \omega_r + \mathrm{i}\,\omega_i$ is the temporal growth rate, and α and β are the dimensionless streamwise and spanwise wavenumbers. The response of the governing equations to disturbance (2.12) is found with the following normal-mode ansatz:

$$\begin{aligned} \{u, v, w, p, \theta^L, \theta^S, D\} = {} & \{u_0, 0, 0, p_0(\zeta), \theta_0^L(\zeta), \theta_0^S(\zeta), 1\} \\ & + \varepsilon f_c \left\{ u_1(\zeta), \frac{f_s}{f_c} v_1(\zeta), w_1, p_1(\zeta), \theta_1^L(\zeta), \theta_1^S(\zeta), d_1 \right\} \mathrm{e}^{\omega t} \end{aligned} \tag{2.13}$$

(plus complex conjugate), where $\varepsilon = \hat{\varepsilon}/2$, $f_c = \mathrm{e}^{\mathrm{i}\alpha x}\cos(\beta y)$ and $f_s = \mathrm{i}\mathrm{e}^{\mathrm{i}\alpha x}\sin(\beta y)$. In addition, we use Squire's transformations, $k^2 = \alpha^2 + \beta^2$ and $kU_1 = \alpha u_1 + \beta v_1$, to reduce the three-dimensional problem to an equivalent two-dimensional problem (e.g. Drazin & Reid 1981), whereas the use of a modified Lagrange function, ϕ, which satisfies the continuity equation at the order $O(\varepsilon)$, and which is defined by

$$U_1 = \phi' + \frac{\alpha}{k} u_0'(\eta_1 + d_1\zeta), \quad w_1 = -\mathrm{i}k\phi, \tag{2.14a,b}$$

reduces the flow field problem to a modified Orr–Sommerfeld problem (prime refers to the ζ-derivative).

By introducing (2.11)–(2.14) into the governing equations (2.5)–(2.10) at the leading order $O(1)$, we obtain the basic state solutions

$$S_0 = (r_\kappa \theta_0^F)^{-1}, \quad u_0 = 2\zeta - \zeta^2, \quad p_0 = \frac{\cos\vartheta}{Fr^2}(1 - \zeta), \tag{2.15a–c}$$

$$\theta_0^L = \zeta\theta_0^F, \quad \theta_0^S = \zeta. \tag{2.16a,b}$$

At order $O(\varepsilon)$, a linearized ordinary differential equation system is instead obtained,

$$(\mathscr{A} - \omega\mathscr{B})\boldsymbol{q} = 0, \tag{2.17}$$

namely a differential generalized eigenvalue problem, where $\boldsymbol{q} = \{\phi, \theta_1^L, \theta_1^S, h_1, \eta_1\}^{\mathrm{T}}$ is a set of eigenfunctions and eigenvectors, $h_1 = \eta_1 + d_1$ quantifies the fluctuations of the free surface, and $\mathscr{A}$ and $\mathscr{B}$ are differential operators that read

$$\mathscr{A} = \begin{pmatrix} \mathscr{D}^2 - \Gamma(u_0\mathscr{D} + 2) & 0 & 0 & 0 & 0 \\ r_\gamma \Lambda k/\alpha & \dfrac{r_\gamma}{\theta_0^F}(\mathscr{D} - \Lambda u_0) & 0 & \sigma_0\zeta & \sigma_0 \\ 0 & 0 & \mathscr{D}_S & 0 & k^2(1+\zeta)S_0 \end{pmatrix}, \tag{2.18}$$

$$\mathscr{B} = St \begin{pmatrix} St^{-1}\chi\mathscr{D} & 0 & 0 & 0 & 0 \\ 1 & 1/\theta_0^F & 0 & -\zeta & \sigma_1 \\ 0 & 0 & 1 & 0 & \sigma_2 \\ & & & & \end{pmatrix}, \tag{2.19}$$

with $\mathscr{D} = \partial_{\zeta\zeta} - k^2$, $\mathscr{D}_S = \partial_{\zeta\zeta} - (S_0 k)^2$, $\Gamma = \mathrm{i}\alpha Re$, $\Lambda = \mathrm{i}\alpha Pe$ and σ_i are ζ-dependent functions, given in appendix A. Finally, the boundary conditions (2.8)–(2.10) read

$$\phi' = -\frac{2\alpha}{k}\eta_1, \quad \phi = \frac{\mathrm{i}\omega\chi}{k}\eta_1, \quad \theta_1^L = \theta_1^S = 0 \quad (\zeta = 0), \tag{2.20a–c}$$

$$r_\gamma S_0 \theta_{1,\zeta}^L - \theta_{1,\zeta}^S + \frac{1+S_0}{S_0}\eta_1 - h_1 = -\omega\eta_1 \quad (\zeta = 0), \tag{2.21}$$

$$k\phi + \alpha h_1 = \mathrm{i}\omega\chi h_1, \quad k\phi'' - \alpha h_1\left(2 + k^2\right) = 0 \quad (\zeta = 1), \tag{2.22a,b}$$

$$\phi''' - (3k + \Gamma)\phi' - \Omega h_1 = \omega\chi Re\phi' \quad (\zeta = 1), \tag{2.23}$$

$$\theta_{1,\zeta}^L = \frac{d_1}{S_0 r_\kappa} \quad (\zeta = 1), \quad \theta_{1,\zeta}^S = \frac{\eta_1}{S_0} \quad (\zeta = -1), \tag{2.24a,b}$$

where the term $\Omega = k\Gamma\alpha^{-1}(\delta + k^2 We^{-2})$ accounts for the effects of the bed inclination and surface tension. Equations (2.17)–(2.24) summarize the physical problem described and solved below.

3. Solutions of the eigenvalue problem

The first equation of the eigenvalue problem (corresponding to the first row of system (2.18), which is the well-known Orr–Sommerfeld equation (henceforth abbreviated to OS), represents the main difficulty of our problem. We have a set of boundary conditions for the free-surface problem (i.e. (2.20*a*,*b*), (2.22)–(2.23)) and, compared with the classical instability problem (e.g. Drazin & Reid 1981; Godreche & Manneville 1998), free-surface problems have in fact attracted less attention. The stability of a viscous film with a non-zero Reynolds number flowing on a rigid plane bed has only recently been solved numerically by Luo & Pozrikidis (2006) in the quasi-steady case, using a Chebyshev tau-QZ algorithm method, whereas its non-normal character has been investigated with the aid of a collocation scheme by Olsson & Henningson (1995). In the following sections, two original solutions (analytical and numerical) of the present thermo-fluid-dynamic problem with a free surface are developed, in order to subsequently study the interfacial instability induced by the differences in the temperature gradients at the liquid–solid interface, the temperature distribution being driven by the near-wall flow field.

3.1. *Quasi-steady approximation: analytical solution*

The quasi-steady approximation implies $St = \chi = 0$. Under this condition, we are able to analytically derive the dispersion relation of the morphological eigenvalue in three steps. Firstly, the eigen-set $\boldsymbol{q}$ is rescaled so that $\eta_1 = 1$.

We first seek an analytical solution of the flow field, governed by the Orr–Sommerfeld-like problem $[\mathscr{D}^2 - \Gamma(u_0\mathscr{D} + 2)]\phi = 0$, which has the general solution in the form $\phi = c_1\phi^{(1)} + c_2\phi^{(2)} + c_3\phi^{(3)} + c_4\phi^{(4)}$. According to the standard nomenclature

(Bender & Orszag 1978), the above equation has an ordinary point, $\zeta_0 = 0$, at the liquid–solid interface and thus, by the Fuchs theorem, each particular solution $\phi^{(j)}$ can be expanded in Taylor series about ζ_0 as

$$\phi^{(j)} = \sum_{i=1}^{\infty} a_{j,i}\zeta^{i-1} \quad (\text{with } j = 1, 4), \tag{3.1}$$

with an infinite radius of convergence (because of the lack of singular points in the problem). The Frobenius method requires us to plug (3.1) back into the OS equation and group the coefficients by power, obtaining a recursive relation for the ith term of series (3.1):

$$a_{j,i} = \frac{\Gamma}{I_1 I_3}\left[\frac{2k^2}{\Gamma} I_3 a_{j,i-2} + 2I_4 a_{j,i-3} + \left(2 - \frac{k^4}{\Gamma} - I_5\right) a_{j,i-4} + k^2(a_{j,i-6} - 2a_{j,i-5})\right] \tag{3.2}$$

where $I_p = (i-p)(i-p-1)$.

Using the boundary conditions at $\zeta = 0$, namely (2.20a,b), we can set $c_3 = 1$ and $c_4 = 0$, so that the solution reduces to the form $\phi = c_1\phi^{(1)} + c_2\phi^{(2)} + \phi^{(3)}$ and the first four terms, $a_{j,i}$, of the Taylor series for $\phi^{(1)}$, $\phi^{(2)}$, $\phi^{(3)}$ (namely $j = 1, 3$ and $i = 1, 4$) are all zero except for $a_{1,3} = a_{2,4} = 1$ and $a_{3,4} = -2\alpha/k$.

The remaining unknowns, c_1, c_2 and h_1, are obtained using the kinematic and dynamic conditions on the free surface, which impose

$$\begin{pmatrix} kL_{10} & kL_{20} & \alpha \\ kL_{12} & kL_{22} & -\alpha\left(2+k^2\right) \\ QL_{11} - L_{13} & QL_{21} - L_{23} & \Omega \end{pmatrix} \begin{pmatrix} c_1 \\ c_2 \\ h_1 \end{pmatrix} = - \begin{pmatrix} kL_{30} \\ kL_{32} \\ QL_{31} - L_{33} \end{pmatrix}, \tag{3.3}$$

where $Q = 3k^2 + \Gamma$ and

$$L_{p0} = \sum_{i=1}^{i=\infty} a_{p,i}, \quad L_{pq} = \sum_{i=1}^{i=\infty}\left[\prod_{r=1}^{r=q}(i-r)\right] a_{p,i}. \tag{3.4a,b}$$

Theoretically, a first requisite for the series representation (3.1) concerns uniform convergence. From Abel's uniform convergence test and the absolute convergence theorem, it follows that the series of functions (3.1) is uniformly convergent in $\zeta \in [0, 1]$ if the numerical series $\sum_{i=1}^{\infty}|\mathrm{Re}[a_{j,i}]|$ and $\sum_{i=1}^{\infty}|\mathrm{Im}[a_{j,i}]|$ are convergent. These latter conditions can be verified using the root test, as it is possible to demonstrate numerically that the limits of $|\mathrm{Re}[a_{j,i}]|^{1/(i-1)}$ and $|\mathrm{Im}[a_{j,i}]|^{1/(i-1)}$ with $i \to \infty$ are smaller than unity.

Another requisite concerns the accuracy of the solutions consequent to the truncation of the series involved in the solutions (3.1)–(3.4). We have verified it by comparing our prediction of h_1 with the results of the numerical solution based on the tau-QZ algorithm developed by Luo & Pozrikidis (2006). If around one hundred terms are adopted in the series, both the magnitude and the phase response agree, in an excellent way, with the numerical predictions (see figure 2). For large values of the parameter $\Gamma = \mathrm{i}\alpha Re$, it is necessary to include many terms in the series. Moreover, for $|\Gamma| \gtrsim 10^3$ the linear system (3.3) becomes ill-conditioned, thus a numerical procedure is required. However, the latter difficulties do not apply to the present problem, where the investigations are limited to $Re < 10^3$ and $(\alpha, \beta) < 1$.

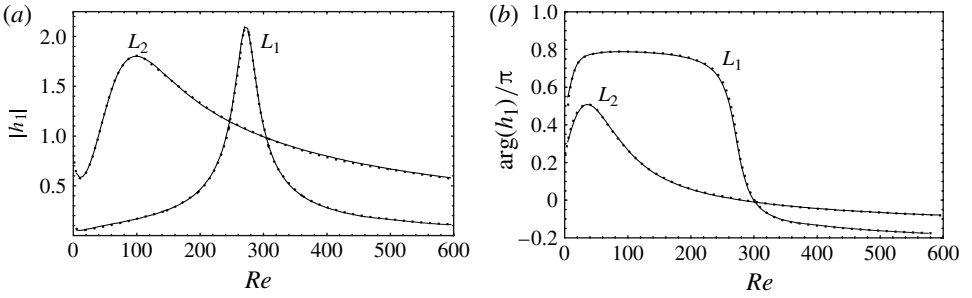

FIGURE 3. Comparison between the present analytical solution (solid lines), and the solution of Luo & Pozrikidis (2006) (dotted lines) for the free-surface fluctuation, h_1, of a water film, in the presence of two different bed corrugation wavelengths: $L_1 = 2$ mm and $L_2 = 5$ mm. The bed inclination is $\vartheta = 30°$.

At the second step, the heat conservation equation in the liquid phase is considered (second row of system (2.18)) which, under the quasi-steady approximation, reads

$$\theta_1^{\prime\prime L} - (\Lambda u_0 + k^2)\theta_1^L = \theta_0^F\,[(1 + d_1\zeta)(\Lambda u_0 - k) - \mathrm{i}kPe\phi]\,. \tag{3.5}$$

Equation (3.5) is a forced parabolic cylinder equation (Abramowitz & Stegun 1965), so its general solution is $\theta_1^L = C_1\Theta_1(\zeta) + C_2\Theta_2(\zeta) + \Theta_p(\zeta)$, with Θ_1 and Θ_2 having the form

$$\left.\begin{aligned}\Theta_1 &= \mathrm{e}^{\mathrm{i}\zeta(\zeta-2)\sqrt{\Lambda}/2} H_\varpi[(\zeta-1)\,(-\Lambda)^{1/4}],\\ \Theta_2 &= \mathrm{e}^{\mathrm{i}\zeta(\zeta-2)\sqrt{\Lambda}/2}\,{}_1F_1\left[-\frac{\varpi}{2}, \frac{1}{2}, \mathrm{i}\,(\zeta-1)^2\sqrt{\Lambda}\right],\end{aligned}\right\} \tag{3.6a,b}$$

where $H_\varpi[\,]$ is the Hermite function, with the parameter ϖ given in appendix B, while ${}_1F_1[\,]$ is the Kummer confluent hypergeometric function. Using the method of variation of parameters, we obtain the particular solution

$$\Theta_p = -\theta_0^F\Theta_1(\zeta)\int^\zeta \frac{f(t)\Theta_2(t)}{W(t)}\,\mathrm{d}t + \theta_0^F\Theta_2(\zeta)\int^\zeta \frac{f(t)\Theta_1(t)}{W(t)}\,\mathrm{d}t, \tag{3.7}$$

where the function $f(\zeta)$ is the term in the square brackets on the right-hand side of (3.5) while $W[\zeta] \equiv W[\Theta_1, \Theta_2]$ is the Wronskian. Furthermore, by using the Liouville–Ostrogradski formula one observes that $W(\zeta) = W[\Theta_1(0), \Theta_2(0)] \equiv W(0) \equiv W_0$, hence the final form of the complete solution reads

$$\theta_1^L = \left(C_1 - \frac{\theta_0^F\mathscr{I}_2(\zeta)}{W_0}\right)\Theta_1(\zeta) + \left(C_2 + \frac{\theta_0^F\mathscr{I}_1(\zeta)}{W_0}\right)\Theta_2(\zeta), \tag{3.8}$$

with $\mathscr{I}_j(\zeta) = \int_0^\zeta f(t)\Theta_j(t)\,\mathrm{d}t$. If (3.6)–(3.8) are substituted in the boundary conditions (2.20*c*), (2.24*a*), the constants C_1 and C_2 can be easily determined.

For the stability analysis, we are interested in the computation of the ζ-derivative of θ_1^L at $\zeta = 0^\pm$, as required by the Stefan equation (2.21). After some algebra we obtain

$$\left.\frac{\partial\theta_1^L}{\partial\zeta}\right|_{\zeta=0^+} = \frac{-\mathscr{I}_2(1) + \mathscr{F}_2 d_1}{\mathscr{F}_1}\theta_0^F, \tag{3.9}$$

where $\mathscr{F}_1$ and $\mathscr{F}_2$ have a cumbersome form, given in appendix B. It suffices to notice here that the second term in the numerator of (3.9) is usually much smaller than the first term, since θ_0^F is small, according to assumption (iv).

From the above solution, it turns out that the computation of the integral $\mathscr{I}_2(1)$ is crucial for the closure of the stability problem. A close analytical form can be achieved by a series representation of the solution Θ_2, so that

$$\mathscr{I}_2(1) = \int_0^1 \left(\sum_{i=0}^{\infty} f_i \zeta^i\right)\left(\sum_{p=0}^{\infty} \frac{\Lambda^{p/2}\mathrm{i}^p}{p!2^p}(2-\zeta)^p\,\zeta^p\right)\left(\sum_{q=0}^{\infty} \frac{\mathrm{i}^q \Lambda^{k/2}\left(-\frac{\varpi}{2}\right)_q}{q!\left(\frac{1}{2}\right)_q}(\zeta-1)^{2q}\right)\mathrm{d}\zeta \tag{3.10}$$

where $(.)_q$ is the Pochhammer symbol (cf. Abramowitz & Stegun 1965), while f_i is derived from the ith Taylor coefficient of the function $f(\zeta)$, and reads

$$f_0 = -(g_0 + k^2), \quad f_1 = -(g_1 + d_1 k^2 + 2\Lambda), \tag{3.11}$$

$$f_2 = -[g_2 + \Lambda(2d_1 - 1)], \quad f_3 = d_1\Lambda - g_3, \quad f_i = -g_i \quad (i = 4, \infty), \tag{3.12}$$

$$g_i = \left[\frac{k\Lambda}{\alpha}(c_1 a_{1,i+1} + c_2 a_{2,i+1} + a_{3,i+1})\right]. \tag{3.13}$$

Collecting the ζ-dependent terms and using the binomial theorem, we obtain

$$\int_0^1 (2-\zeta)^p\,\zeta^{p+i}\,(\zeta-1)^{2q}\,\mathrm{d}\zeta = \sum_{r=0}^{p}\sum_{s=0}^{2q} \frac{\binom{p}{r}\binom{2q}{s}2^r(-1)^{p-r-s}}{1+i+2p+s-r} = \frac{(-1)^p(2q)!(i+2p)!}{(i+2q+2p+1)!}\boldsymbol{F}_{ipq}, \tag{3.14}$$

where the third-order tensor $\boldsymbol{F}_{ipq} = {}_2F_1[-1-i-2q-2p, -p, -i-2p, 2]$. Hence, using (3.14) in (3.10), we finally obtain

$$\mathscr{I}_2(1) = \sum_{i=0}^{\infty}\sum_{p=0}^{\infty}\sum_{q=0}^{\infty} \frac{f_i\left(-\frac{\varpi}{2}\right)_q \mathrm{i}^{q+p}\Lambda^{\frac{p+q}{2}}(-1)^p(2q)!(i+2p)!}{2^p\left(\frac{1}{2}\right)_q p!q!(i+2q+2p+1)!}\boldsymbol{F}_{ipq}. \tag{3.15}$$

It is worth observing that, for large values of Pe, the series (3.15) requires a high truncation value of the index p and q, thus the calculation of $\mathscr{I}_2$ could be quite cumbersome. In this case, an alternative recursive form can be achieved by applying the Frobenius method in a similar manner to the OS problem. In this way, one obtains $\theta_1^L|_{\zeta=0^+} = -T_{21}/T_{11} + \theta_0^F d_1/T_{11}$, where $T_{j1} = \sum_{i=1}^{N}(i-1)t_{j,i}$, with $(j = 1, 2)$ and

$$t_{j,i} = \frac{1}{(j-1)(j-2)}\left[k^2 t_{j,i-2} + 2\Lambda t_{j,i-3} - \Lambda t_{j,i-4} + G_{j,i-2}\right], \tag{3.16}$$

$$t_{1,1} = t_{2,1} = t_{2,2} = G_{1,i} = 0, \quad t_{1,2} = 1, \quad G_{2,i} = f_i. \tag{3.17a–f}$$

The third step of this analysis is the solution of the heat equation in the solid phase (third row of system (2.18)), which reads $\mathscr{D}_S\theta_1^S + k^2(1+\zeta)S_0 = 0$. Considering boundary conditions (2.20*c*, 2.24*b*), the solution is

$$\theta_1^S = \frac{1+\zeta-\mathrm{e}^{-kS_0\zeta}+\mathrm{e}^{2kS_0}(1+\zeta-\mathrm{e}^{kS_0\zeta})}{S_0(1+\mathrm{e}^{2kS_0})}, \tag{3.18}$$

from which we obtain $\theta_1'^S|_{\zeta=0^-} = S_0^{-1} - k\tanh(kS_0)$. A crude analysis of the latter result suggests that $\theta_1'^S|_{\zeta=0^-} \sim S_0^{-1} - k^2 S_0$, provided k is not too large, so the thermal gradient in the solid phase changes from being a destabilizing to a stabilizing process at a critical wavenumber $k_c \sim S_0^{-1}$, namely when the wavelength perturbation is comparable to the solid depth. Through (2.15*a*), we observe that for $\theta_0^F = 0.05$ one obtains $k_c \sim 0.035$, which is comparable to the values that affect the morphological instability, as will be shown in § 4 (see figure 5). It appears that, although the dynamic response of the solid phase has never been accounted for in previous work, it appears to be significant for the correct computation of the growth factor.

If solutions for $\theta_1'^S|_{\zeta=0^-}$ and $\theta_1'^L|_{\zeta=0^+}$ are substituted in the Stefan condition (2.21), we finally come to the claimed dispersion relation

$$\omega = r_\kappa \theta_0^F \left[\frac{I_2(1)}{\mathscr{F}_1} + d_1 \left(1 - \frac{\mathscr{F}_2}{\mathscr{F}_1} \right) - k \tanh\left(\frac{k}{r_\kappa \theta_0^F} \right) \right]. \tag{3.19}$$

To summarize, we emphasize the main novelties encompassed in (3.19): (i) it is an analytical solution; (ii) it accounts for the morphological instability of a liquid–solid interface with a laminar open-channel flow without any other restrictions on the Reynolds number; (ii) the perturbative response of the solid thermodynamics is also considered, as testified by the last term in (3.19).

3.2. *Numerical solution*

The solution given in the previous section needs to be tested using a fully unsteady numerical solver, in order to test the validity of the quasi-steady approximation, as well as the accuracy of the analytical method. To this end, we adopt a spectral-Galerkin method based on the analysis by Giannakis, Fischer & Rosner (2009) and Camporeale, Canuto & Ridolfi (2011), to which the reader can refer for further details. This tool will also be used in § 4 to obtain the whole spectrum of eigenvalues.

In order to recast the differential eigenvalue problem introduced in § 2 (i.e. (2.17)) in the algebraic form $\boldsymbol{A}\boldsymbol{w} = \omega \boldsymbol{B}\boldsymbol{w}$, we discretize the problem using a spectral Galerkin technique which prevents the onset of spurious eigenvalues (e.g. Canuto *et al.* 2006). Even this technique consists of three main steps. First, a modal representation of the solution is adopted, where the eigenfunctions $\{\phi, \theta_1^L, \theta_1^S\}$ appearing in $\boldsymbol{q}$ are expanded in the (truncated) spectral form

$$\phi = \sum_{i=-3}^{N} \phi_i \Phi_i^\phi(y), \quad \theta_1^L = \sum_{i=-1}^{N} \theta_i^L \Phi_i^L(y), \quad \theta_1^S = \sum_{i=-1}^{N} \theta_i^S \Phi_i^L(y), \tag{3.20}$$

$\{\Phi_i^\phi, \Phi_i^L, \Phi_i^S\}$ being three sets of trial functions, whilst $\{\phi_i, \theta_i^L, \theta_i^S, \eta_1, h_1\} =: \boldsymbol{w}$ represents the unknown complex eigenvector. For numerical convenience, the vertical coordinate is further mapped to the range $y \in [-1, 1]$ for both phases, using $y = 2\zeta - 1$ (for $\zeta > 0$) and $y = 2\zeta + 1$ (for $\zeta < 0$).

Second, the original eigenvalue problem is multiplied by a set of test functions,

$$V = \{v \in C^2([-1, 1]) : v(-1) = v'(-1) = 0, v(1) = 0\}, \tag{3.21}$$

and integrated over the domain $[-1, 1]$. The repeated use of integration by parts allows the fourth and third derivatives to be reduced to second-order derivatives; in addition, the normal component of the dynamic boundary condition (2.23) is incorporated in the mass and stiffness operators in the so-called weak form (Canuto *et al.* 2006), through the boundary term that arises from the integration by parts.

Third, the correct choice of the trial and test functions enables the use of the remaining boundary conditions to be set in a strong form, that is, as additional rows in the ultimate algebraic system. Inspired by Shen (1994), we consider the set of polynomials

$$\varphi_i = \sqrt{i+\frac{3}{2}}\left(\frac{L_{i+3}-L_{i+1}}{(2i+3)(2i+5)}-\frac{L_{i+1}-L_{i-1}}{(2i+1)(2i+3)}\right), \quad i\in[1,N-3], \tag{3.22}$$

where $L_i(y)$ denotes the ith Legendre polynomial. These functions are obtained by integrating each Legendre polynomial twice, while enforcing zero boundary conditions at $y=\pm1$ for the function and its first derivative. The set of functions in (3.22) completes the set of solutions of the classical OS problem, where the boundary conditions are all homogeneous. Here, instead, we need to add six low-degree polynomials, in order to accommodate non-vanishing boundary conditions, which are

$$\varphi_{-3}=\frac{1}{4}(y+1)^2 \quad \varphi_{-2}=\frac{1}{4}(3-y^2-2y), \quad \varphi_{-1}=\frac{1}{1}(1-y^2), \tag{3.23}$$

$$\varphi_0^{\phi}=\frac{1}{2}+\frac{3}{4}y-\frac{1}{4}y^3, \quad \varphi_0^{L}=\frac{1+y}{2}, \quad \varphi_0^{L}=\frac{1-y}{2}. \tag{3.24}$$

It is straightforward to verify that the trial and test spaces for the present problem are arranged as

$$\boldsymbol{\Phi}_i^{\phi}=\{\varphi_{-3},\varphi_{-2},\varphi_{-1},\varphi_0^{\phi},\varphi_i\}, \quad \boldsymbol{\Phi}_i^{L}=\left\{-2\varphi_{-1},\varphi_0^{L},\frac{\mathrm{d}\varphi_i}{\mathrm{d}y}\right\}, \tag{3.25}$$

$$\boldsymbol{\Phi}_i^{S}=\left\{-2\varphi_{-1},\varphi_0^{S},\frac{\mathrm{d}\varphi_i}{\mathrm{d}y}\right\}, \quad V=\left\{\varphi_0^{\phi},\varphi_i,\varphi_0^{L},\frac{\mathrm{d}\varphi_i}{\mathrm{d}y},\varphi_0^{S},\frac{\mathrm{d}\varphi_i}{\mathrm{d}y}\right\}, \tag{3.26}$$

where, with the aid of the proprieties of Legendre polynomials, we can use the following formula for the y-derivatives:

$$\frac{\mathrm{d}\varphi_i}{\mathrm{d}y}=\frac{L_{i+2}-L_i}{\sqrt{2(2i+3)}}. \tag{3.27}$$

We recall that the use of Lagrange polynomials allows the fourth-order derivative term in the OS equation (i.e. the most critical from a computational view) to be transformed into a unitary matrix (after twice integrating by parts, one in fact obtains $\int_{-1}^{1}\varphi_i''\varphi_j''\,\mathrm{d}y=\delta_{ij}$), thus reducing the risk of roundoff, typical in collocation schemes. The given algebraic problem is easily solved by means of the QZ algorithm. We emphasize that the above technique has three fundamental advantages: (i) it ensures high spectral accuracy and convergence in the solution provided the truncation number N is of order $O(10^2)$; (ii) it avoids spurious eigenvalues; (iii) it provides the entire spectrum and related eigenfunctions.

3.3. *Validation of the quasi-steady approximation*

We finally provide an evaluation of the accuracy of the main outcome of the analytical solution, namely the eigenvalue ω obtained under the quasi-steady approximation. Figure 4 shows a comparison between the spectral solution of the morphological eigenvalue and solution (3.19) for a fixed set of $\{\alpha,\theta_0^F,\vartheta\}$. We recall that the quasi-steady approximation is equivalent to setting $St=0$ in the numerical scheme. The behaviours of the growth factor, $\omega_r:=\mathrm{Re}(\omega)$, and the phase velocity, $c_p=-\mathrm{Im}(\omega)/\alpha$, versus the quantity αRe are given in figure 4(*a*,*b*), respectively, where the numerical

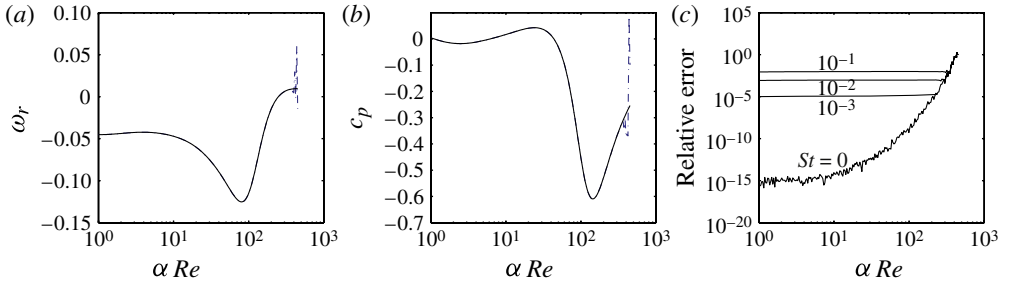

FIGURE 4. Comparison between analytical and numerical solution of the morphological mode. (*a*) Growth factor, (*b*) phase velocity: numerical (solid line), analytical (dashed line) in the case $St = 0$. The curves practically coincide till the boundary of validity of our formulation. (*c*) Relative error of $|\omega|$. $\alpha = k = 0.2$, $\theta_0^F = 0.05$, $\vartheta = \pi/360$, $Pr = 13$, water case.

solution with $St = 0$ (solid line) is compared with the analytical solution (dashed line). It is evident that up to $\alpha Re \sim 400$, analytical and numerical solutions are indistinguishable. Figure 4(*c*) shows the relative error of $|\omega|$ between analytical and numerical prediction for different Stefan numbers ($St = 0, 10^{-3}, 10^{-2}, 10^{-1}$). At $St = 0$ the agreement is remarkable, being the relative difference close to the numerical precision for low Reynolds number and increasing with a very low rate (notice the log-scale). For non-vanishing Stefan numbers, the relative errors are almost independent of the Reynolds number, increasing with St, but small nevertheless. Even at the uppermost condition ($St = O(10^{-1})$), the effects of unsteadiness are practically negligible, thus the quasi-steady approximation is always acceptable.

4. Results

We investigate the case of pure water at standard conditions, i.e. $Pr = Pe/Re = 13$, $r_\kappa = 0.68$, $\rho_L = 999$ kg m^{-3}, $\nu = 1.751 \times 10^{-6}$ m^2 s^{-1} and $\sigma = 0.727$ N m^{-1}. The independent parameters governing the dispersion relation (3.19) reduce to Re, k, α, ϑ, θ_0^F. Notice that the Froude number is linked to the previous ones, with the aid of the Nusselt solution, through the relationship $2Fr^2 \cos\vartheta = Re$.

We first focus on two-dimensional perturbations, namely $k = \alpha$. Figure 5 shows the stability analysis for five different values of the bed inclination ϑ, spanning the ranges $Re \in [1\text{–}10^3]$ and $\alpha \in [0\text{–}0.4]$. Some results are immediately evident. First, the water–ice system exhibits well-defined domains of morphological instability for all the values of bed inclination, in the range 0.5–30°. Second, the domain of instability, as well as the maximum value of the temporal growth rate, decrease with the increase in the bed inclination. The magnitude of $\omega_{max} := \max(\omega_r)$ in fact decreases from 5×10^{-3}, for $\vartheta = \pi/360$, to 8×10^{-4}, for $\vartheta = \pi/50$ and 7×10^{-6}, for $\vartheta = \pi/6$. Third, the unstable waves migrate upstream (i.e. $c_p < 0$). Finally, the free-surface fluctuation h_1 is almost in phase with the bed surface shape, in the region of instability; it is also interesting to observe that the occurrence of the maximum instability does not coincide with the maximum amplitude of the free-surface fluctuation. As the surface temperature θ_0^F increases, the instability domain slightly moves towards lower values of Re (for small k, ω is in fact proportional to θ_0^F: see (3.19)), but the previous picture does not change in a qualitative way.

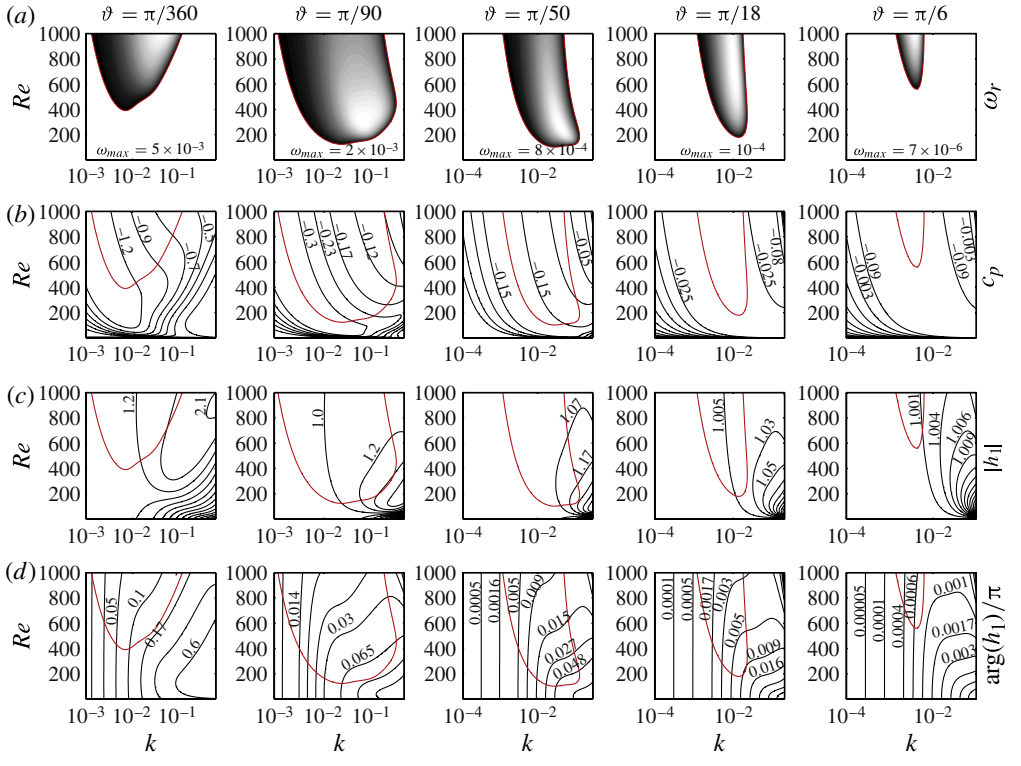

FIGURE 5. The instability domain in the plane (α, Re), for five different values of the bed inclination, ϑ: (*a*) temporal growth rate (black zone indicates $\omega_r > 0$); (*b*) phase velocity; (*c*) magnitude of the free-surface fluctuation; (*d*) phase lag of the free-surface fluctuation ($\theta_0^F = 0.05$, water case). The red lines mark the marginal stability curves.

A useful indication of the onset of morphodynamic instability is given by the smallest values of the Reynolds number, such that $\omega_r > 0$, expressed as a function of the bed inclination and the surface temperature (but regardless of the wavenumber). This critical value, Re_c, corresponds to the lower limit of the marginal stability curves (red lines) reported in figure 5, and its behaviour is depicted in figure 6 for values of $\theta_0^F = [0.05\text{–}0.55]$. Greater values for the dimensionless surface temperature are not considered because of the constraints imposed by the assumption (iv), as noted in § 2. It can be observed that Re_c exhibits a minimum at intermediate values of the bed inclination ranging between 4 and 10 degrees. Note, incidentally, that such slopes are frequently encountered in non-crevassed glaciers. It also appears that the instability domain increases with θ_0^F, and the values of Re_c tend to be less dependent on the slope with the increase in surface temperature. In the same figure, a comparison with the marginal curve for the surface instability (dashed curve), makes it evident that the latter occurs at smaller Reynolds numbers than the morphological one. While evaluating the dashed curve, we observed excellent agreement (error $<1\,\%$) between the theoretical formula $Re_c = 1.25 \cot\vartheta$ and our spectral method, thus providing a numerical validation of the theory of Yih (1963).

Taking advantage of the computational technique introduced in the previous section, we are also able to investigate the whole spectrum of the eigenvalue problem (2.17) and the physical meaning of its branches. The interest in solving an eigenvalue

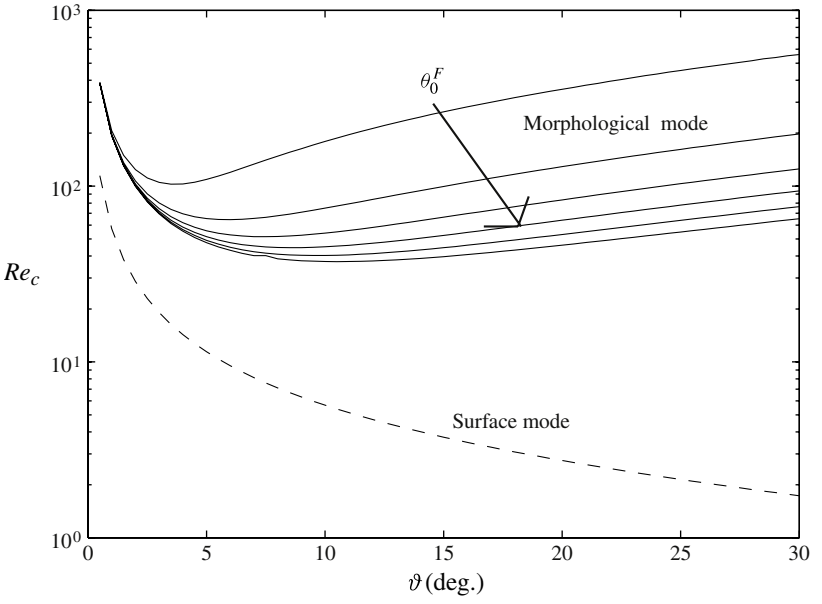

FIGURE 6. The behaviour of the critical Reynolds number Re_c versus the bed inclination ϑ and the basic free-surface temperature ($\theta_0^F = [0.05-0.55]$). The dashed line marks the surface mode.

problem lies in two ways of investigating the instability itself, namely the modal and non-modal approach or, equivalently, in the two ways of considering the instability, asymptotically or transiently. In the former approach, one is only interested in the least stable eigenvalue in order to understand whether the system is asymptotically unstable in time and, if it is, what kind of instability develops. In the latter, the transient instabilities are also an object of investigation; thus, one is interested in the computation of the whole spectrum of eigenvalues and the associated eigenfunctions in order to tackle the initial value problem as well (Schmid 2007). This last kind of analysis has received a great impetus in recent years (e.g. Trefethen & Embree 2005), because of its physical consequences, and because it does not exclude but embeds the results of the modal approach.

The study of transient behaviour will be the subject of future work, but it is instructive to comment on the eigenvalue distribution in the complex plane displayed in figure 7 (the corresponding eigenfunctions can also be shown but are not given for the sake of space). We recall that the real part of the eigenvalues represents the growth rate while the imaginary part is related to the phase velocity by $c_p = -\omega_i/k$. The computation has been made for a fixed set of parameters, corresponding to unstable conditions. The different physical nature of the eigenvalues has been identified as follows. Since the diagonalization in Jordan form of the matrices $\boldsymbol{A}$ and $\boldsymbol{B}$ is precluded in practice, a distinct separation of eigenvalues is a hard task. However, we have recognized the physical origin of each branch by developing separate analyses for the different sub-problems. For example, the hydrodynamic modes were identified by the solution of the OS problem alone, and so on. The result of this identification analysis is given in figure 7.

Two principal branches are evident: an upper and a lower one. The upper one, with phase velocity close to zero and real part invariably negative, reflects the presence

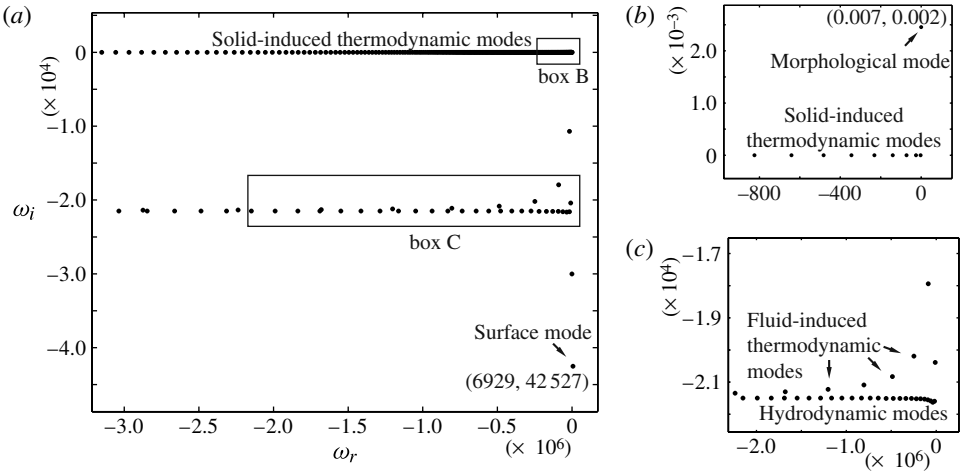

FIGURE 7. Spectrum in the complex plane. (*a*) Full portrait of the first 100 eigenvalues; (*b*) close-up of box B; (*c*) close-up of box C. $Re = 400$, $\alpha = 0.02$, $\beta = 0$, $\theta_0^F = 0.05$, $\vartheta = 3.6°$, $St = 10^{-3}$.

of the solid phase (i.e. solid-induced thermodynamic modes). At the rightmost bound of this branch, one can find the morphological mode (see box B) that is instead unstable ($\omega_r > 0$) and upstream-migrating ($\omega_i > 0$, $c_p < 0$). The lower branch is instead associated to the fluid phase. In particular, one can distinguish the hydrodynamic modes and the (fluid-induced) thermodynamic modes. The hydrodynamic modes are invariably stable, turbulent instabilities are in fact damped and are represented by a horizontal row of points. This set of points is exactly the so-called S-branch of the spectrum of the classical OS equation, which is associated to the modes transported with the mean bulk velocity, equal to two-thirds of the surface velocity (Grosch & Salwen 1968). Our results are in full agreement with this prediction, in fact: $-\chi\omega_i/k = 0.66$. The fluid-induced thermodynamic modes are marked in box C, where it is evident that they follow a curved branch, with variable phase velocity, which asymptotically merges the hydrodynamic modes moving leftwards. Finally, the surface mode, induced by the open-channel boundary conditions, is evident in the bottom right corner. It is the most unstable one, as expected.

We conclude this section with a brief analysis of tri-dimensional effects. It suffices to focus on the morphological mode only, thus the quasi-steady approximation is again adopted. Squire's theorem, a classical result of hydrodynamic instability theory, states that waves with the maximum growth rate are invariably two-dimensional. In the analysis of the OS problem it is therefore sufficient to study two-dimensional perturbations (e.g. Drazin & Reid 1981). It is interesting to observe that, although the present problem has some resemblances to the classical Orr–Sommerfeld problem, its open-channel nature and the coupling with the thermo-morphodynamic processes preclude one from extending the validity of Squire's theorem to the present morphological instability. This point is elucidated in figure 8, where the contour plots of the growth rate are reported in the plane (α, β) for different values of Re and ϑ. A remarkable result is that the most unstable waveforms, marked by crosses in the figure, are two-dimensional ($\beta \sim 0$) only at very low values of Reynolds number and slope. With the increase in Re and ϑ, three-dimensionality of the most unstable waveforms increases greatly. This effect is due to the inertial terms in the equations

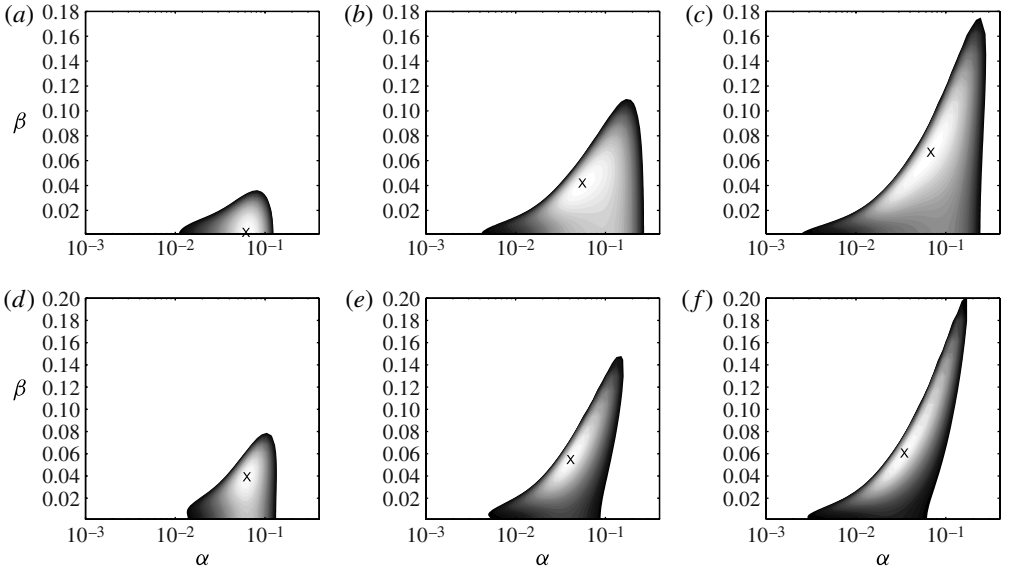

FIGURE 8. Contour plot of the growth rate in the plane (α, β), for $Re = \{200, 400, 600\}$ and $\theta_0^F = 0.05$. (*a*)–(*c*) $\vartheta = 1°$; (*d*)–(*f*) $\vartheta = 3.6°$. Crosses mark the maximum values. (*a*,*d*) $Re = 200$; (*b*,*e*) $Re = 400$; (*c*,*f*) $Re = 600$.

which trigger spanwise gradients in the flow field induced by the free surface. At high Reynolds numbers, three-dimensionality appears so important that, for some values of the longitudinal wavenumber, α, only three-dimensional waveforms are unstable (e.g. figure 8*f*, at $\alpha = 10^{-1}$). Again, it is remarkable to notice that this picture is in agreement with the patterns performed by ice ripples observed on glaciers, where a dominant longitudinal wavelength usually combines with a longer transversal structure.

5. Discussion

A quantitative description of the instability phenomena has been given in the previous section. Now, we investigate the physical processes that contribute to the onset of morphodynamic instability. For this purpose, we remove some key elements from the complete dynamics one by one, in order to study their effect on the instability. In particular we focus on (i) the role of inertial forces, (ii) the dynamics of the free surface at the liquid–gas interface, and (iii) the boundary condition of conservation of the heat flux. The study of point (i) requires the structure of the fluid dynamic equations to be changed, whereas we only use the boundary conditions to investigate points (ii) and (iii).

5.1. *The role of the inertial forces*

Neglecting the inertial forces in the Navier–Stokes equation for a generic two-dimensional flow (namely the Stokes approximation) leads to a biharmonic equation for the stream-function (Batchelor 2000, p. 224). In the present framework, the Orr–Sommerfeld equation therefore reduces to a differential equation with constant coefficients

$$\phi^{iv} - 2k^2\phi'' + k^4\phi = 0, \tag{5.1}$$

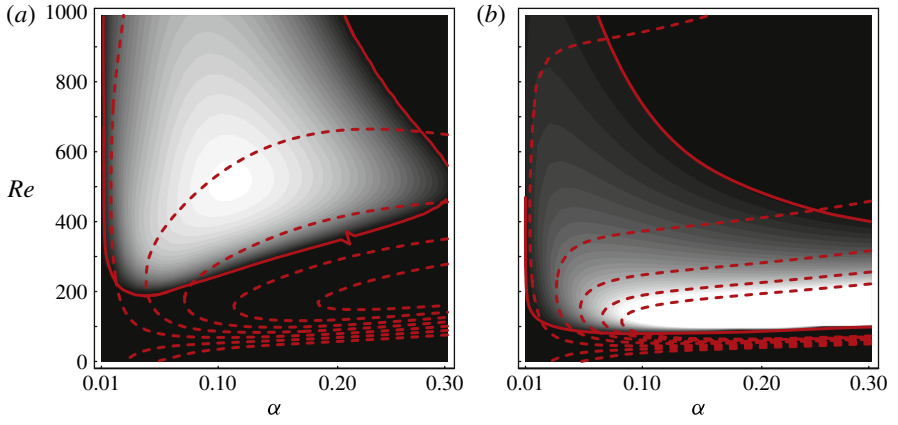

FIGURE 9. (Colour online) Distribution of the growth rate (grey shades) and the magnitude of the free-surface fluctuations (dashed lines) in the plane (α, Re) (the solid line marks the instability area). (*a*) Complete solution ($\max[\omega_r] = 0.0029$); (*b*) Stokes approximation ($\max[\omega_r] = 0.069$).

the boundary conditions being the same as those of the complete problem. After some algebra, one can obtain the solution of (5.1) which, for the sake of space, we do not give here (but see Wang 1981). The solution of the free-surface fluctuation reads

$$h_1 = \frac{-2e^k k\alpha(3k + k^3 + \Gamma + k\Gamma) + k\,[3 + (k-6)k - \Gamma] + \Gamma}{\alpha\Upsilon - 2k^3\Omega + \alpha\left(3k - 3k^2 - 2k^4 + \Gamma\right)\cosh(2k) + k^2\Omega\sinh(2k)}, \tag{5.2}$$

where $\Upsilon = 3(k + k^2 - 2k^3 - 2k^5 + k^6) - \Gamma(1 + 2k^2 + 2k^4)$.

With the aim of understanding the role of the inertial forces in the onset of instability, we have forced the Stokes solution for non-negligible values of the Reynolds number in order to make a qualitative comparison of the instability response with the complete solution, as shown in figure 9. From these results, it is evident that the inertial terms are not necessary for instability, even though neglecting them leads to an overestimate of ω_r, the wrong localization of the domain of the most unstable waves and an underestimate of the critical Reynolds number. A comparison of the free-surface fluctuations confirms that the complete solution coincides with the Stokes approximation (i.e. (5.2)) for very low Reynolds numbers only (i.e. $Re \simeq O(1)$). Figure 9(*b*) also shows the existence of a strong correlation between the growth rate distribution and the free-surface behaviour when inertial forces are neglected. This is in contrast with the complete solution, where the maximum values of ω_r and $|h_1|$ are located at different parts of the plane (α, Re). This discrepancy can be related to the higher value of $|h_1|$, in the Stokes approximation, owing to the loss of the advective terms, as is better explained in the next section.

In the most recent literature on viscous film dynamics (Bontozoglou & Papapolymerou 1997; Luo & Pozrikidis 2006), the inertial forces have been emphasized to be crucial for a correct description of the phenomenon of a kind of 'resonance', namely the strong amplification of the free-surface fluctuations detectable for suitable wavenumbers of the wall corrugation. This phenomenon was also expected to have important implications on heat and mass transfer processes. From the present analysis, it instead emerges that resonance is not essential for morphological interface instability. In fact, although the resonance phenomenon can be recognized through

the inspection of the dashed lines in figure 3(*a*) (i.e. $|h_1| > 1$ if $\alpha > 0.1$ and $100 < Re < 500$), the lack of correlation between $\max(\omega_r)$ and $\max|h_1|$ implies that resonance does not play a fundamental role in the onset of morphodynamic instability.

5.2. *The role of free-surface dynamics and heat conservation at the boundaries*

In order to understand the mechanism that is responsible for morphological instability, it is useful to depict the spatial behaviour of some key variables on the physical plane $\{x, z\}$, using transformations (2.11). In particular, we concentrate on the perturbed parts of the flow field, $\boldsymbol{u}_1$, temperature distribution, θ_1, and vorticity distribution, φ_1. Notice that, in the two-dimensional case, vorticity reduces to the vector $\boldsymbol{\nabla} \times \boldsymbol{u} = (0, \Psi(x, \zeta), 0)$, where Ψ is described by an advection–diffusion equation which – under the usual structure of perturbation (i.e. $\Psi = \varphi_0(\zeta) + \varepsilon \mathrm{e}^{\omega_r t}\varphi_1(\zeta)\cos(\alpha x + \omega_i t)$) – gives the fluctuating part of the vorticity at $O(\varepsilon)$, φ_1, to be modelled by an equation that is very similar to (3.5). Hence, vorticity and temperature are subjected to the same diffusion and convection mechanisms, even though they are constrained by different boundary conditions (e.g. Batchelor 2000). The computation of vorticity fluctuation is therefore straightforward and, using the Lagrange function, it reads

$$\varphi_1 = \phi'' - k^2\phi + 4d_1 u_0' + (1 + d_1\zeta)u_0''. \tag{5.3}$$

Figure 10(*a*) shows the behaviour of the variables $\boldsymbol{u}_1$, θ_1, φ_1 along a wavelength for the complete problem solved in § 3. First, we distinguish the presence of two contour-rotating cells of vorticity, which are generated at the liquid–solid interface and then diffused and convected in the upstream direction. The temperature and vorticity patterns are almost aligned with each other, even though the temperature exhibits a more pronounced symmetry because of the absence of the wall-generation mechanism. The phase shift of the warmest and coldest regions, with respect to the wall, is consistent with the destabilizing condition, which needs a net flux heat so that ridges grow and troughs melt (e.g. Thorsness & Hanratty 1979). Moreover, the localization of the warmest (coldest) region downstream (upstream) of the trough explains the upstream phase velocity of instability, as recognized in the previous section. Finally, we can note the presence of relatively strong vertical components of the perturbed velocity.

In order to clarify the links between the flow field and the temperature distribution and the role played by the free surface in the onset of instability, let us study three modifications of the problem investigated so far: (i) the free surface is virtually replaced by a flat rigid wall (problem *Fw*); (ii) the free surface is replaced by a corrugated rigid wall parallel to the liquid–surface interface (problem *Cw*); (iii) the free-surface fluctuations are completely neglected and, therefore, the free surface remains flat, as observable at the basic state (problem *Fn*). Problem *Fw* reproduces the conditions inside a closed-channel flow where the flat upper wall warms the fluid and the lower wall freezes it. In problem *Cw* the free-surface dynamics is also completely removed, but an undulating streamline distortion is maintained due to the presence of a fictitious moving corrugated upper wall. Finally, in problem *Fn*, the presence of a free surface is maintained, but it is unperturbed, so the streamline patterns are more similar to the closed channel.

It is evident that problem *Fw* is the only physically realistic case but, in spite of their artificiality, the other two are also useful in shedding light on the influence of the upper boundary conditions. In fact, for all three new problems, the differential model is the same as in the original problem, and only the kinematic and dynamical conditions change, leading the basic flow of problems *Fw* and *Cw* to be modified

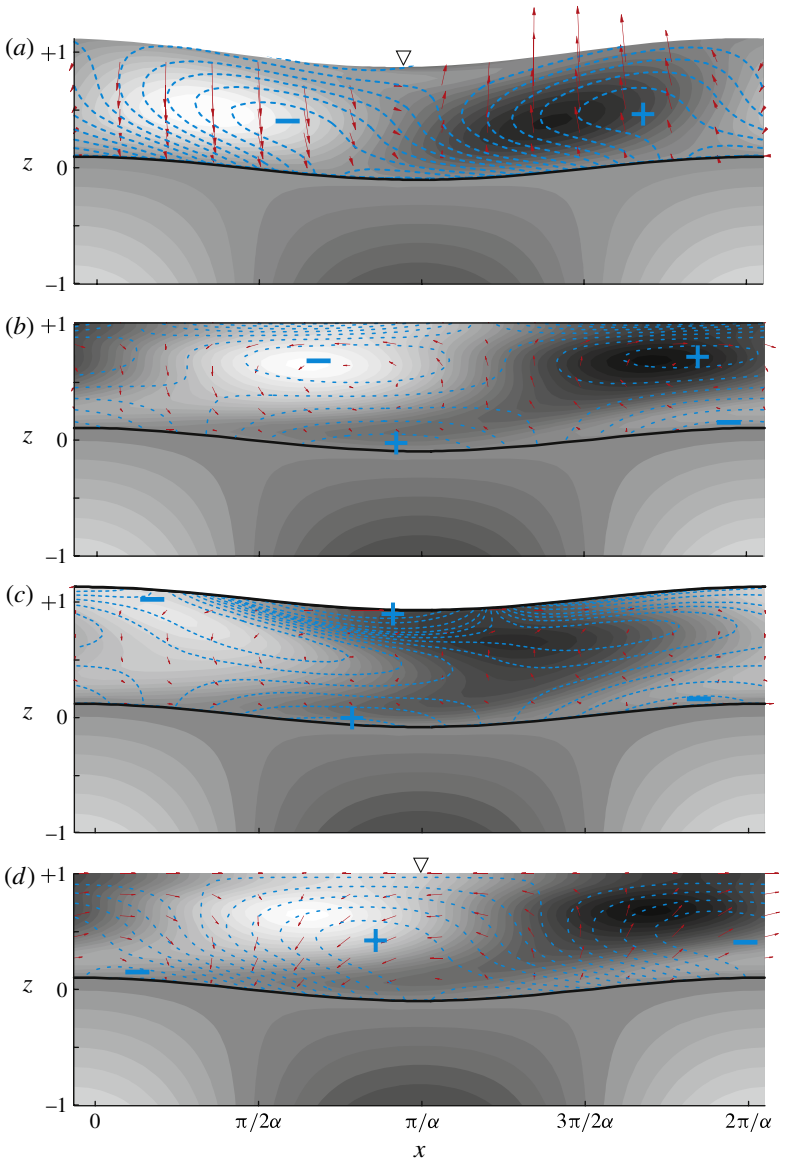

FIGURE 10. (Colour online) A comparison of the perturbed values of the flow field (arrows), temperature distribution (warmer in white, colder in black), and vorticity (lines, the symbols + and − refer to the sign) between the original problem (*a*) and problems *Fw* (*b*), *Cw* (*c*), and *Fn* (*d*). The scale factor for the velocities differs between the panels. $Re = 300$, $\alpha = 0.07$, $\vartheta = \pi/90$, $\theta_0^F = 0.05$, $\varepsilon = 0.025$.

to $u_0 = 4(\zeta - \zeta^2)$, whereas the values at order $O(\varepsilon)$ are

$$\text{problem } Fw\text{: } h_1 = 0, \quad \phi(1) = 0 \quad \phi'(1) = 0, \tag{5.4}$$

$$\text{problem } Cw\text{: } h_1 = 1, \quad \phi(1) = 0 \quad \phi'(1) = 0, \tag{5.5}$$

$$\text{problem } Fn\text{: } h_1 = 0, \quad \phi(1) = 0 \quad \phi''(1) = 0. \tag{5.6}$$

If the stability analysis is developed for the three new problems, it demonstrates that the liquid–solid interface is stable in all cases. This is a key point, because it implies that the free surface – correctly modelled by the original problem – plays an essential role in the instability process, which is absent in the three variations. Similarly to figure 10(*a*), figure 10(*b–d*) shows the perturbed parts of the flow field, temperature distribution, and vorticity distribution, for the problems (*Fw*, *Cw*, and *Fn*). It is possible to see that the correlation between vorticity and temperature is also performed to some extent in the modified problems; however, in these cases, the cells are more in phase with the bed corrugation. Furthermore, we observe that for problems *Fw* and *Cw* (i.e. figure 10*b*,*c*) the upstream convection and upward diffusion of the vorticity generated at the liquid–solid interface is precluded by the effect of the upper wall, which generates new vorticity that diffuses downwards. Generally, the phase lag of the flow field structure, with respect to the bed corrugation, appears to be damped if the boundary conditions acquire some symmetry in the coordinate ζ.

If the flow field is focused on, one observes that the only unstable problem (i.e. the original one) is characterized by a relatively high vertical component of the perturbed velocity (figure 10*a*) whereas, in all the other cases, the horizontal component is usually predominant. This important difference can easily be explained. In the original problem, the free-surface fluctuations, combined with the bed corrugation, induce a strong distortion of the streamlines, but do not significantly alter the profile of the base longitudinal flow, $u_0(\zeta)$; therefore, the perturbation of the velocity vector is mostly directed in the vertical direction. On the other hand, the presence of a flat upper boundary (problems *Fw* and *Fn*) and/or the constraint of a null velocity at the upper boundary (problems *Fw* and *Cw*) inhibit the formation of a sufficiently large vertical component of the velocity. In addition, for the case of the closed-channel problem *Fw* (panel *b*), the high long-stream variations in the cross-section are balanced by high variations in U_1, because of the continuity of the flux.

From the above analysis it emerges that free-surface dynamics plays a fundamental role in the onset of instability, the mechanisms thereof being explained as follows. The kinematic and dynamic conditions induce a surface fluctuation and a consequent streamline distortion with a dramatic increase in the vertical component of velocity. This kinematic structure favours the heat transport between the warmer free surface and the colder liquid–solid interface, with a phase shift that is forced by the ζ-asymmetry in the boundary conditions. Finally, the phase shift in the heat flux provides the destabilizing condition, as previously mentioned. The importance of the vertical velocity on the heat transport is also visible in the linearized governing equations: in heat conservation equation (3.5), the effect of the perturbed flow field is only felt through the terms d_1 and $w_1 = -\mathrm{i}k\phi$, which are contained in the non-homogeneous forcing part, whereas the component U_1 gives no contribution.

In the previous section, we observed that, in the region of instability, $0 < \arg(h_1) < \pi/2$ and, generally, $\arg(h_1)$ decreases with the increase in the Reynolds number (see figure 5, last row of panels). It follows that the phase response of the free surface is a stabilizing factor while, as previously described, its amplitude response is a destabilizing factor (see also the term proportional to d_1 in (3.19)). This is consistent with three other results: (i) the existence of a particular physical condition, described by the curve of marginal stability, where two mechanisms are in equilibrium; (ii) the evidence of a stronger correlation between the contour plots of ω_r and $|h_1|$ in the case of the Stokes approximation, i.e. the loss of inertial forces induces an increase in the amplitude response of the free surface with a further steepening of the streamlines; (iii) a negative temporal growth rate, if the free-surface phase response is neglected.

We conclude the present discussion with a comment about the approximations made on the thermal boundary conditions at $\zeta = \pm 1$. A rigorous application of the heat conservation law at the free surface would also require the gas response to also be modelled. In that case, the correct linearized boundary condition would be equivalent to a linear combination of the Dirichlet and Neumann conditions (i.e. a Robin condition), rather than only a Neumann condition as used here. A similar argument could also be applied to the boundary condition at the solid bottom ($\zeta = -1$). However, we have observed that if conditions (2.24) are replaced by Dirichlet conditions, no significant differences in the numerical value of the dispersion relations emerge and, due to linearity, neither does the correct Robin boundary condition. It follows that our assumption of the Neumann boundary condition for the temperature field (the only approximation in the present theory that is not based on scaling considerations) does not have any significant impact on the obtained results.

6. Conclusions

The present work elucidates the significance of free-surface dynamics on the onset of morphodynamic instability of a liquid–solid interface bounding a laminar open-channel flow at large Reynolds numbers. In order to show the key role played by the free surface, the analytical solution of both the Orr–Sommerfeld equation, for the open-channel problem with $Re = 1$–10^3, and of the linearized heat conservation equations, for the liquid and solid phase, are obtained. The flow field solution has been successfully validated through a comparison with the numerical solution developed by Luo & Pozrikidis (2006). No approximations have been made for the flow and heat fields, the only exception being (i) to consider, in the analytical solution, the fluid dynamics and thermodynamics to quickly adjust to the bed configuration, (ii) to assume a dynamical equilibrium between solid and liquid at the steady state, and (iii) to neglect the thermodynamics of the upper gas layer. The first approximation is justified provided $St \ll 1$, the latter two if the thickness of the solid layer is not too small and the surface temperature of the liquid is not too high. We also developed a fully numerical solution with a spectral Galerkin method, which permitted us to test the validity of the analytical theory and to analyse the physical meaning of the whole eigenvalue portrait. We developed our theory taking water as an example, but it is also extendable to other incompressible Newtonian fluids.

As noted, free-surface dynamics has been found to be the essential ingredient that induces the formation of unstable wavelets on a liquid–solid interface. In this sense, the result is consistent with the analysis by Feltham & Worster (1999), where no instabilities occurred when the free surface was removed. A quantitative comparison with other simplified problems has also suggested that the key mechanism lies in the distortion of the streamlines induced by the free-surface dynamics. In particular, its amplitude response is a destabilizing factor while its phase response is a stabilizing factor. In contrast, the inertia forces do not appear to be crucial for the onset of instability, but are instead crucial for the correct localization of the marginal stability curve.

The features of the unstable ‘ice waves’ depend on the bed inclination, Reynolds number and the basic free-surface temperature. The results show that single wavelets migrate upstream, in a similar manner to the instabilities observed by Gilpin (1981) in pipes under a transition regime. The critical Reynolds number decreases with an increase in the surface temperature with minimum values when the bed inclination is

in the range 5–15°. Three-dimensional effects appear to be relevant with increasing Reynolds number.

All these findings have good correspondence in the formation of ice ripples on glacier surfaces, induced by flow of meltwater. Coming back to figure 1, we can now attempt a theoretical estimate of the selected pattern. Assuming average summer conditions at the surface of the Ciardoney glacier (solar radiation 1200 W m^{-2}, ice albedo 0.75) and a roughly simplified energy balance at the liquid–solid interface, just involving radiation and ice latent heat ($\lambda = 3.34 \times 10^5$ J kg^{-1}), it follows that an ice surface 250 m long on a 4 % slope generates a melt 'Nusselt' film with $Re = 150$. If heat conduction in the liquid and lateral self-radiation of the glacier were also accounted for, the same flow would be obtained by a shorter surface (up to −50 %), as observed during our field measurements. If we also set $\theta_0^F = 0.01$ (estimated by our field measurements), the dispersion relation (3.19) provides that the most unstable pattern is characterized by $L_x \sim 9$ cm and $L_y \sim 1$ m, in good agreement with data reported in figure 1. Despite the high uncertainty in the above crude estimate, it is remarkable that the present theory is able to correctly reproduce the order of magnitude of the pattern instability of ice ripples. Although one could guess that similar patterns are also induced by sublimation, through air katabatic flows, both processes are more likely to cooperate in inducing instability. However, given the pattern alignment with the micro-relief structure of the surface, meltwater probably dominates. This point surely deserves further investigation.

Further improvements in the present analysis would be welcomed. Two issues deserve particular attention: to understand the role of air dynamics at large Reynolds numbers (i.e. relaxing assumption (iii)) and to develop a non-modal analysis in the spirit of Schmid (2007) and Camporeale & Ridolfi (2011), in order to investigate possible transient behaviours and their effects on two- and three-dimensional instabilities.

Acknowledgements

We would like to thank Professor C. Canuto for the fruitful discussions and his remarkable insights, L. Mercalli for his assistance on the Ciardoney glacier, and the CRT (Cassa di Risparmio di Torino) Foundation for financial support.

Appendix A. Coefficients of systems (2.18), (2.19)

$$\sigma_0 = r_\gamma(k - \Lambda u_0), \quad \sigma_1 = 1 - \zeta - s, \quad \sigma_2 = -(1+\zeta)/S_0. \tag{A 1}$$

Appendix B. Expression for the function $\mathscr{F}_1$, $\mathscr{F}_2$ and ϖ reported in § 3.1

$$\mathscr{F}_1 = {}_1F_1\left[-\frac{\varpi}{2}, \frac{1}{2}, \mathrm{i}\sqrt{\Lambda}\right], \quad \mathscr{F}_2 = \left[\mathscr{F}_4 - \mathscr{F}_3\mathscr{F}_5\left(k^2 + \frac{\mathrm{i}\sqrt{\Lambda}+\Lambda}{2}\right)\right] \mathrm{e}^{-(\mathrm{i}\sqrt{\Lambda})/2}, \tag{B 1}$$

with

$$\mathscr{F}_3 = {}_1F_1\left[\varpi_3, \frac{3}{2}, \mathrm{i}\sqrt{\Lambda}\right], \quad \mathscr{F}_4 = \mathscr{F}_1 \cdot {}_1F_1\left[\varpi_3, \frac{1}{2}, \mathrm{i}\sqrt{\Lambda}\right], \quad \mathscr{F}_5 = {}_1F_1\left[\varpi_5, \frac{3}{2}, \mathrm{i}\sqrt{\Lambda}\right], \tag{B 2}$$

and

$$\varpi_a = -\frac{\mathrm{i}(k^2 + a\mathrm{i}\sqrt{\Lambda} + \Lambda)}{4\sqrt{\Lambda}}, \quad \varpi = -2\varpi_1. \tag{B 3}$$

REFERENCES

ABRAMOWITZ, M. & STEGUN, I. A. 1965 *Handbook of Mathematical Functions: With Formulas, Graphs and Mathematical Tables*. Dover.

ASHTON, G. D. & KENNEDY, J. F. 1972 Ripples on underside of river ice covers. *Proc. ASCE* **98** (HY9), 1603–1624.

BATCHELOR, G. K. 2000 *An Introduction to Fluid Mechanics*. Cambridge University Press.

BENDER, C. & ORSZAG, S. A. 1978 *Advanced Mathematical Methods for Scientists and Engineers*. McGraw-Hill.

BENJAMIN, T. B. 1957 Wave formation in laminar flow down an inclined plane. *J. Fluid Mech.* **2**, 554–574.

BLUMBERG, P. N. & CURL, R. L. 1974 Experimental and theoretical studies of dissolution roughness. *J. Fluid Mech.* **65**, 735–751.

BONTOZOGLOU, V. & PAPAPOLYMEROU, G. 1997 Laminar flow down a wavy incline. *Intl J. Multiphase Flow* **23**, 69–79.

CAMPOREALE, C., CANUTO, C. & RIDOLFI, L. 2011 A spectral approach for the stability analysis of turbulent open-channel flows over granular beds. *Theor. Comput. Fluid Dyn.* **26** (1), 51–80.

CAMPOREALE, C., PERONA, P., PORPORATO, A. & RIDOLFI, L. 2007 Hierarchy of models for meandering rivers and related morphodynamic processes. *Rev. Geophys.* **45**, RG1001.

CAMPOREALE, C. & RIDOLFI, L. 2011 Modal versus nonmodal linear stability analysis of river dunes. *Phys. Fluids* **23** (10), 104102.

CANUTO, C., HUSSAINI, M. Y., QUARTERONI, A. & ZANG, T. A. 2006 *Spectral Methods. Fundamentals in Single Domains*. Springer.

COLEMAN, S. E. & EDLING, B. 2000 Sand wavelets in laminar open-channel flows. *J. Hydraul. Res.* **38** (5), 331–338.

COLOMBINI, M. & STOCCHINO, A. 2005 Coupling or decoupling bed and flow dynamics: fast and slow sediment waves at high Froude numbers. *Phys. Fluids* **17** (3), 036602.

DEVAUCHELLE, O., MALVERTI, L., LAJEUNESSE, E., LAGRÉE, P. Y., JOSSERAND, C. & NGUYEN THU-LAM, K. D. 2010 Stability of bedforms in laminar flows with free surface: from bars to ripples. *J. Fluid Mech.* **642**, 329–348.

DRAZIN, P. G. & REID, W. H. 1981 *Hydrodynamic Stability*. Cambridge University Press.

EXNER, F. M. 1925 *Über Die Wechselwirkung Zwischen Wasser und Geschiebe in Flüssen,* vol. 14, pp. 165–180. Akademie der Wissenschaften, Wien (in German).

FELTHAM, D. L. & WORSTER, M. G. 1999 Flow-induced morphological instability of a mushy layer. *J. Fluid Mech.* **391**, 337–357.

FERGUSON, R. I. 1973 Sinuosity of supraglacial streams. *Geol. Soc. Am. Bull.* **84**, 251–256.

GIANNAKIS, D., FISCHER, P. & ROSNER, R. 2009 A spectral Galerkin method for the coupled Orr–Sommerfeld and induction equations for free-surface MHD. *J. Comput. Phys.* **228** (4), 1188–1233.

GILPIN, R. R. 1981 Ice formation in a pipe containing flows in the transition and turbulent regimes. *J. Heat Transfer* **103**, 363–368.

GILPIN, T., HIRATA, R. R. & CHENG, K. C. 1980 Wave formation and heat transfer at an ice–water interface in the presence of a turbulent flow. *J. Fluid Mech.* **99**, 619–640.

GODRECHE, C. & MANNEVILLE, P. (Eds) 1998 *Hydrodynamics and Nonlinear Instabilities*. Cambridge University Press.

GROSCH, C. E. & SALWEN, H. 1968 The stability of steady and time-dependent plane Poiseuille flow. *J. Fluid Mech.* **34**, 177–194.

HUTTER, K. 1983 *Theoretical Glaciology: Material Science of Ice and the Mechanics of Glaciers and Ice Sheets*. Springer.

KASER, G., COGLEY, J. G., DYURGEROV, M. B., MEIER, M. F. & OHMURA, A. 2006 Mass balance of glaciers and ice caps: consensus estimates for 1961–2004. *Geophys. Res. Lett.* **33** (19), L19501.

LOCK, G. S. H 1990 *The Growth and Decay of Ice*. Cambridge University Press.

LUO, H. & POZRIKIDIS, C. 2006 Effect of inertia on film flow over oblique and three-dimensional corrugations. *Phys. Fluids* **18**, 078107.

NEUFELD, J. A., GOLDSTEIN, R. E. & WORSTER, M. G. 2010 On the mechanisms of icicle evolution. *J. Fluid Mech.* **647**, 287–308.

OGAWA, N. & FURUKAWA, Y. 2002 Surface instability of icicles. *Phys. Rev.* E **66** (4, part 1), 041202.

OLSSON, P. J. & HENNINGSON, D. S. 1995 Optimal disturbance growth in water table flow. *Stud. Appl. Maths* **94**, 183–210.

PARKER, G. 1975 Meandering of supraglacial melt streams. *Water Resour. Res.* **11** (4), 551–552.

SCHMID, P. J. 2007 Nonmodal stability theory. *Annu. Rev. Fluid Mech.* **39**, 129–162.

SCHMID, P. J. & HENNINGSON, D. S. 2001 *Stability and Transition in Shear Flows*, *Applied Mathematical Sciences*, vol. 142. Springer.

SEMINARA, G. 2010 Fluvial sedimentary patterns. *Annu. Rev. Fluid Mech.* **42**, 43–66.

SHEN, J. 1994 Efficient spectral-Galerkin methods. Part I. Direct solvers for the second and fourth order equations using Legendre polynomials. *SIAM J. Sci. Comput.* **15** (6), 1489–1505.

SHORT, M. B., BAYGENTS, J. C. & GOLDSTEIN, R. E. 2006 A free-boundary theory for the shape of the ideal dripping icicle. *Phys. Fluids* **18** (8), 083101.

STEFAN, J. 1891 Über die Theorie der Eisbildung, insbesondere über die Eisbildung im Polarmeere. *Ann. Phys. Chem.* **42**, 269–286.

THOMAS, R. R. 1979 Size of scallops and ripples formed by flowing water. *Nature* **277**, 281–283.

THORSNESS, C. B. & HANRATTY, T. J. 1979 Stability of dissolving or depositing surfaces. *AIChE* **25**, 697–701.

TREFETHEN, L. N. & EMBREE, M. 2005 *Spectra and Pseudospectra*. Princeton University Press.

UENO, K. 2003 Pattern formation in crystal growth under parabolic shear flow. *Phys. Rev.* E **68** (2, part 1), 021603.

UENO, K., FARZANEH, M., YAMAGUCHI, S. & TSUJI, H. 2010 Numerical and experimental verification of a theoretical model of ripple formation in ice growth under supercooled water film flow. *Fluid Dyn. Res.* **42** (2), 025508.

WANG, C. Y. 1981 Liquid film flowing slowly down a wavy incline. *AIChE J.* **27** (2), 207–212.

WIERSCHEM, A. & AKSEL, N. 2003 Instability of a liquid film flowing down an inclined wavy plane. *Physica* D **186**, 221–237.

WORSTER, M. G. 1992 Instabilities of the liquid and mushy layers. *J. Fluid Mech.* **237**, 649–669.

WORSTER, M. G. 2000 Solidification of fluids. In *Perspectives in Fluid Dynamics: A Collective Introduction to Current Research* (ed. M. G. Worster, G. K. Batchelor & H. K. Moffat). Cambridge University Press (chapter 8).

YIH, C. S. 1963 Stability of liquid flow down an inclined plane. *Phys. Fluids* **6**, 321–334.